GEOCHEMISTRY, GEOPHYSICS, GEOSYSTEMS, VOL. ???, XXXX, DOI:10.1029/,

Lower mantle structure from paleogeographically constrained dynamic Earth models

Dan J. Bower,[1] Michael Gurnis,[1] Maria Seton,[2]

D. J. Bower, Seismological Laboratory, California Institute of Technology, Pasadena, CA 91125, USA (danb@gps.caltech.edu)

M. Gurnis, Seismological Laboratory, California Institute of Technology, Pasadena, CA 91125, USA

M. Seton, EarthByte Group, School of Geosciences, University of Sydney, NSW 2006, Australia

[1]Seismological Laboratory, California Institute of Technology, Pasadena, CA 91125, USA

[2]EarthByte Group, School of Geosciences, University of Sydney, NSW 2006, Australia

Abstract. Seismic tomography reveals two large, low-shear velocity provinces (LLSVPs) beneath Africa and the Pacific Ocean. These structures may have existed for several 100 Myrs and are likely compositionally distinct based on observed seismic characteristics interpreted in light of geodynamic models and mineral physics constraints. We investigate the dynamics of the LLSVPs through the use of evolutionary models of thermochemical convection from 250 Ma to present day. We use a spherical convection model in which the anomalous structures have a high bulk modulus, consistent with seismic interpretation. A new progressive assimilation method incorporates constraints from paleogeography using a refined plate history model (with 1 Myr time spacing) to guide the thermal structure of the lithosphere and steer the thermal evolution of slabs in the uppermost mantle.

The thermochemical structures deform and migrate along the core-mantle boundary (CMB) through coupling to plate motions and in response to slab stresses. The models produce a ridge-like anomaly beneath Africa and a rounded pile beneath the Pacific Ocean which at present day agrees with tomography, waveform modeling, and other geodynamic studies. Plumes emanate from the margins of the domes and ridges of thickened boundary layer between the domes. Dense and viscous slabs can undermine the stability of high bulk modulus structures at the CMB. High bulk modulus structures are not necessarily required to satisfy dynamic constraints on the LLSVPs.

1. Introduction

Seismic tomography (Fig. 1a,b) reveals two large, low-shear velocity provinces (LLSVPs) at the base of the mantle beneath Africa and the Pacific Ocean with approximately a degree-two pattern. These structures contain 1.5–2.4 vol. % and $\approx$ 2 mass % of the mantle and occupy almost 20% of the surface area at the core-mantle boundary (CMB) [e.g., *Hernlund and Houser*, 2008; *Burke et al.*, 2008].

A thermochemical origin can explain anti-correlated shear wave and bulk sound velocity anomalies [*Su and Dziewonski*, 1997; *Masters et al.*, 2000], putative anti-correlated shear wave and density anomalies [*Ishii and Tromp*, 1999, 2004], multipathing for waves sampling its steep edges [*Ni et al.*, 2002], and geological inferences of stability since 300–200 Ma [*Burke and Torsvik*, 2004]. Exclusively thermal models can also explain the long-wavelength heterogeneity revealed in tomography [*Schuberth et al.*, 2009, 2012], strong gradients in shear wave velocity [*Schuberth et al.*, 2009], and a variety of hot spot characteristics [*Davies and Davies*, 2009]. Thermal effects may dominate density and shear wave heterogeneity [*Simmons et al.*, 2009] and clusters of small plumes, possibly with distinct chemistry, may explain the African and Pacific structures [*Schubert et al.*, 2004].

Waveform modeling identifies the finer-scale structure and refines the geographical extent of the LLSVPs. This technique is particularly useful to address ambiguity in tomography models by resolving the vertical extent of the structures and the wavespeed reduction and thickness of the basal layer.

Ritsema et al. [1998] present compelling evidence for a large mid-mantle structure beneath Africa by satisfying travel-time data for S, ScS, and SKS, along a corridor from the

Drake passage to the Hindu Kush. The African LLSVP rises 1500 km above the CMB with an S wavespeed reduction of 3%. This is also supported by the first arrival cross over of SKS to S from South American events to world-wide standard seismographic network (WWSSN) stations in Africa [*Ni et al.*, 1999]. These early studies identify strong shear velocity gradients at the edges and top of the structure. *Ni et al.* [2002] attribute SKS waveform complexity to in-plane (2-D) multipathing and use the travel-time delays to determine a boundary width of less than 50 km. They further suggest the eastern edge of the bulk of the anomaly is tilted toward the northeast, in agreement with some tomography models [*Ritsema et al.*, 1999] (Fig. 1c). Alternatively, *Wang and Wen* [2007a] use more data from events northeast of the anomaly to argue that this flank tilts to the center and the basal layer extends farther northeast.

The thickness and velocity reduction of the basal layer at the CMB beneath the African structure remains contentious. Beneath the eastern part of the South Atlantic, *Wen et al.* [2001] propose a 300-km-thick anomaly with much lower S wavespeeds linearly decreasing from -2% at the top to about -10% at the base [also see *Wen*, 2002]. P and S core reflected phases support this interpretation [*Simmons and Grand*, 2002]. *Wen* [2001] extend this feature beneath the Indian Ocean by modeling several corridors of data and ascribe travel-time delays to variations in layer thickness. However, others favor a moderate basal layer with -3% S wavespeed [e.g., *Ni and Helmberger*, 2003a, b]. This later model attributes some of the travel-time delays to the mid-mantle structure, particularly for SKS paths, and thus the basal wavespeed reduction is less. The geographical footprint on the CMB is the same regardless of the vertical extent of the anomaly [e.g., *Wang and Wen*, 2004].

Ni and Helmberger [2003c] model the 3-D geometry of the African LLSVP as a ridge-like structure approximately 1200 km high and 1000 km wide that extends 7000 km along the CMB from Africa to the Indian Ocean. By contrast, the more extreme basal layer model is compatible with a limited and localized mid-mantle extent [e.g., *Wen*, 2006]. Definitive confirmation of either model is limited by sparse data coverage for azimuths other than the Drake Passage to Hindu Kush corridor [*Helmberger and Ni*, 2005]. 3-D multipathing along strike of the African structure [*Ni et al.*, 2005; *To et al.*, 2005] or extreme wavespeed reductions in the basal layer can both explain delayed S-wave postcursors. New seismic tools are being developed to address such ambiguities by helping to distinguish between in-plane (2-D) multipathing caused by horizontal structure and out-of-plane (3-D) multipathing due to vertical structure [*Sun et al.*, 2009].

The African structure also exhibits small-scale features. Ultralow-velocity zones (ULVZs) are detected at the edges of the LLSVP, with one extending at least 800 km along the eastern boundary beneath central Africa [*Helmberger et al.*, 2000; *Ni and Helmberger*, 2001a]. Another is located between Madagscar and Africa [*Wen*, 2000] and a third beneath Tristan [*Ni and Helmberger*, 2001b]. Shear wave anisotropy has been interpreted as revealing complex flow occuring at the edges [*Wang and Wen*, 2007b] suggesting strong interactions between the LLSVP and ambient mantle. Recently, *Sun et al.* [2010] provide waveform evidence for a small plume with a diameter less than 150 km emanating from the top of the structure beneath southern Africa.

The Pacific LLSVP is less well imaged than its African counterpart because of source receiver geometry and its location beneath the vast Pacific Ocean. *He and Wen* [2009] construct a comprehensive model along a great arc from east Eurasia to South America

using S, Sd, ScS, SKS, and SKKS phases. Their model divides the Pacific LLSVP into a western and eastern province separated by an ≈ 700 km gap beneath the Fiji Islands. The western province rises 740 km above the CMB and is 1050 km wide at the base, with edges conjectured to be steeper than the African structure. The eastern section is 340–650 km high and 1800 km wide. This overall geometry is also evident in tomography (e.g., Fig. 1d). Each province resembles a trapezoid with a lateral dimension that increases with depth with an S wavespeed reduction of 3% and 5% in the interior and basal portions, respectively [*He and Wen*, 2009]. Another cross section from Fiji-Tonga to California uses multibounce S and ScS phases to overcome the lack of stations in the ocean basin [*Liu et al.*, 2011]. These authors report an overall average height of 600 km with an average anomalous S velocity of -2% and make note of its geometric complexity in comparison to the apparently more simple African LLSVP.

Sharp edges are identified at the margins of the Pacific structure to the south [*To et al.*, 2005], east [e.g., *Liu et al.*, 2011], and west [*Takeuchi et al.*, 2008]. The northeast boundary abuts an ULVZ or a slow basal layer which is overlain by a high-velocity region (≈ 120 km thickness) that extends further to the northeast [*He et al.*, 2006; *He and Wen*, 2009]. Numerous ULVZs are detected at the southwest margin [see *Thorne and Garnero*, 2004] and a few are situated beneath the LLSVP [e.g., *Liu et al.*, 2011].

Geodynamic calculations have attempted to reproduce the long-wavelength morphology of the LLSVPs; a linear ridge-like feature beneath Africa and a rounded pile beneath the Pacific Ocean. Early 3-D Cartesian thermochemical convection studies with temperature-dependent viscosity [*Tackley*, 1998, 2002] and laboratory experiments [e.g., *Davaille et al.*, 2002; *Jellinek and Manga*, 2002; *Olson and Kincaid*, 1991] only produce ubiquitous ridge-

like features. However, large thermally-induced viscosity contrasts ($> 10^4$) can produce pools of dense material that persist for several Gyr [*Deschamps and Tackley*, 2008]. Spherical geometry alone is unable to produce rounded piles without assigning a higher intrinsic viscosity to the LLSVPs, and ridges and piles do not coexist [*McNamara and Zhong*, 2004]. Low Rayleigh number ($\sim 10^5$) isoviscous calculations with a density interface reveal interface topography with a similar form to piles although the interface is continuous and the "piles" are not isolated [*Oldham and Davies*, 2004].

Plate motion history can control the location and morphology of the LLSVPs as shown in models [*McNamara and Zhong*, 2005] that use a global tectonic reconstruction since 119 Ma [*Lithgow-Bertelloni and Richards*, 1998]. *Zhang et al.* [2010] recently extended this model by constructing a few, conjectural plate stages back to 450 Ma to further investigate LLSVP mobility and stability using incompressible models with a high-density basal layer. They argue that prior to Pangea formation the African mantle was dominated by downwellings from convergence between Laurussia and Gondwana. The downwellings pushed the chemically distinct material south of Gondwana and into the Pacific hemisphere, forming a single pile. Subsequent circum-Pangea subduction, particularly on the southeast side of the supercontinent, split the chemical pile into two, forming the African LLSVP. This suggests the Pacific structure has existed since the Early Paleozoic whereas the bulk of the African structure formed at 230 Ma, about 100 Myr after the assembly of Pangea. *Zhong et al.* [2007] show that this implies an interaction of degree-one mantle convection and the supercontinent cycle.

The reconstructed eruption sites of large igneous provinces (LIPs) (since 300 Ma) [*Burke and Torsvik*, 2004; *Burke et al.*, 2008], major hotspots [*Burke et al.*, 2008], and kimberlites

(since 320 Ma) [*Torsvik et al.*, 2010] correlate with the edges of the African and Pacific LLSVPs. *Burke et al.* [2008] therefore propose that the boundaries of the LLSVPs at the CMB are "Plume Generation Zones" (PGZs). This hypothesis suggests that the African and Pacific structures have been independent and stable since before 300 Ma and may be insensitive to plate motions, contrary to the models of *Zhang et al.* [2010]. Furthermore, the existence of older LIPs (since 2.5 Ga) suggest LLSVPs earlier in Earth history, although they are not necessarily derived from the same structures that exist today [*Burke et al.*, 2008].

A chemically distinct component with a high bulk modulus (high-K) generates structures that satisfy geodynamic and seismic constraints on the LLSVPs [*Tan and Gurnis*, 2005, 2007; *Sun et al.*, 2007]. Recent calculations in a spherical geometry reveal the propensity for stronger plumes to develop at the edges of such domes compared to their tops, providing a potential dynamic model for the PGZs [*Tan et al.*, 2011]. Since high-K structures rely on a balance between thermal and compositional buoyancy the net density anomaly (relative to ambient mantle) is often small. While this facilitates domes with high relief and sharp, steep boundaries, it may render the structures passive to the circulation induced by plate motions. Subduction zone geometry influences the location of the domes and therefore it may be problematic to maintain the spatial stability of high-K structures for several hundred million years [*Tan et al.*, 2011].

In this study we investigate the stability and morphology of LLSVPs with high-K in a mantle constrained by the tectonic evolution of the lithosphere from 250 Ma to the present. Our models incorporate several advances: (1) a new global tectonic reconstruction [*Seton et al.*, 2012] with continuously closing plate polygons [*Gurnis et al.*, 2012] that

has much finer spatial and temporal resolution while being consistent with the details of global geology; (2) constraints on the thermal evolution of the lithosphere through the assimilation of reconstructed seafloor ages; (3) steering the evolution of slabs in the uppermost mantle using the new tectonic reconstruction and a thermal slab model through progressive data assimilation.

2. Numerical models

2.1. Governing equations

We apply the extended Boussinesq and Boussinesq approximation (hereafter EX and BO, respectively) [e.g., *Ita and King*, 1994] to model thermochemical convection using finite element models. The finite element problem is solved with CitcomS [*Zhong et al.*, 2000, 2008] which is modified to incorporate a depth-dependent chemical density anomaly [e.g., *Tan and Gurnis*, 2007] to simulate the effect of a high bulk modulus material. The equation for the conservation of mass is:

$$\nabla \cdot \mathbf{u} = 0 \tag{1}$$

where $\mathbf{u}$ is velocity. The non-dimensional momentum equation is:

$$-\nabla P + \nabla \cdot \underline{\tau} = (\Gamma^{-1}\overline{\Delta\rho_{ch}}C - \bar{\alpha}T)Ra\bar{g}\hat{\mathbf{r}} \tag{2}$$

where P is dynamic pressure, $\underline{\tau}$ deviatoric stress tensor, α coefficient of thermal expansion, T temperature, $\Delta\rho_{ch}$ chemical density, C concentration of compositionally distinct material, Ra thermal Rayleigh number, g gravity, and $\hat{\mathbf{r}}$ radial unit vector. Overbars denote input parameters that only depend on radius and "0" subscripts denote dimensional reference values (Table 1). Maximum thermal density anomaly $\Gamma = \rho_0\alpha_0\Delta T$, where ρ_0 is density and ΔT is the temperature drop across the mantle. ΔT is the superadiabatic tem-

perature drop for BO models and additionally includes an adiabatic temperature change for EX models.

The Grüneisen parameter (γ) is used *a priori* to construct the depth-dependent chemical density ($\overline{\Delta\rho_{ch}}$) by integrating the self-compression equations for two chemistries with different bulk moduli and zero-pressure density [see *Tan and Gurnis*, 2007, for details]. We report the chemical density anomaly at the CMB ($\delta\rho_{ch}$) and the bulk modulus anomaly (δK) (Table 2). The usual definition of the buoyancy number, B is recovered for depth-independent chemical density anomaly, $B = \Gamma^{-1}\overline{\Delta\rho_{ch}}$.

The Rayleigh number is defined as:

$$Ra = \frac{\rho_0 \alpha_0 \Delta T {R_0}^3 g_0}{\eta_0 \kappa_0} \tag{3}$$

where R_0 is Earth radius, η_0 viscosity, and κ_0 thermal diffusivity (Table 2). This definition uses the Earth radius rather than mantle thickness and is thus about an order of magnitude larger than the normal definition.

The (non-dimensional) energy equation is:

$$\bar{c_p}\frac{\partial T}{\partial t} = -\bar{c_p}\mathbf{u}\cdot\nabla T + \nabla\cdot(\bar{c_p}\bar{\kappa}\nabla T) - Di(T+T_S)\bar{\alpha}\bar{g}u_r + \frac{Di}{Ra}\underline{\tau}:\underline{\dot{\epsilon}} + H \tag{4}$$

where c_p is heat capacity, $Di = \alpha_0 g_0 R_0 / c_{p0}$ is dissipation number, T_S is surface temperature, $\underline{\dot{\epsilon}}$ is strain rate tensor, and H is internal heating rate (Table 1).

The usual definition for the Boussinesq approximation ignores depth-dependent material properties and heating terms involving Di. However, since high-K structures necessitate pressure-dependent parameters, our BO models only neglect the additional heating terms ($Di = 0$).

The equation for chemical advection is:

$$\frac{\partial C}{\partial t} + (\mathbf{u} \cdot \nabla) C = 0. \tag{5}$$

We advect tracers representing the chemical components using a predictor-corrector scheme [*McNamara and Zhong*, 2004] and determine composition using the ratio method [*Tackley and King*, 2003].

2.2. Model setup

The full sphere is constructed of 12 caps, each with 128×128×64 elements, giving a total of $\sim$ 12.6 million elements. Radial mesh refinement provides the highest resolution of 18 km in the boundary layers and a minimum resolution of 90 km in the mid-mantle.

We define the reference thermal expansion coefficient $\alpha_0 = 3 \times 10^{-5}$ K^{-1} [*Stacey*, 1977], which is comparable with perovskite at ambient conditions [*Katsura et al.*, 2009]. High-K domes can form for a range of thermal expansion profiles that decrease with pressure from the surface to the CMB (see *Tan and Gurnis* [2007], Fig. 3). For EX models, the profile is derived from experimental data for $MgSiO_3$ perovskite and the thermal expansion coefficient decreases more strongly in the upper mantle than the lower mantle ("M09", Table 2) [*Mosenfelder et al.*, 2009]. The dimensional thermal expansion coefficients at the surface and CMB are 3.9×10^{-5} K^{-1} and 1×10^{-5} K^{-1}, respectively. For BO models, the thermal expansion coefficient decreases linearly from 3×10^{-5} K^{-1} at the surface to 1.5×10^{-5} K^{-1} at the CMB ("linear", Table 2).

We adopt a purely diffusion creep constitutive relation which is likely to be appropriate for the lower mantle [*Karato and Li*, 1992]. Dislocation creep and yielding are critical for the motion of plates and slabs [*Billen and Hirth*, 2007; *Stadler et al.*, 2010]. However,

because of assimilated plate kinematics and slab structure in the upper mantle (see next section) we effectively remove the need to include these complexities. Viscosity (non-dimensional) is composition dependent:

$$\eta(T, r) = \eta_0(r)(1 + \eta_C C) \exp[E(0.5 - T)] \tag{6}$$

where $\eta_0(r)$ is a radially dependent prefactor, η_C is intrinsic compositional viscosity prefactor, and E is non-dimensional activation energy. $\eta_0(r) = 1$ for the lithosphere (0–100 km depth) and $\eta_0(r) = 1/30$ for the upper mantle (100–670 km depth). For the lower mantle $\eta_0(r)$ increases linearly from 2.0 at 670 km depth to η_Z at the CMB (Table 2) [e.g., *Zhang et al.*, 2010]. This pressure-induced viscosity increase offsets the decrease caused by the adiabatic temperature gradient for EX models. $E = 172$ kJ mol^{-1} generates 10^3 viscosity variation due to temperature (Table 1).

We apply a free slip and isothermal ($T = 1$) boundary condition at the CMB and a kinematic and isothermal ($T = 0$) boundary condition at the top surface. The upper thermal boundary layer is characterized by large velocity gradients and high viscosity due to the temperature-dependent rheology and the imposed 30× step increase from the upper mantle. In the EX framework viscous dissipation produces intense localized heating at plate boundaries. This produces large gradients in strain rate and viscosity which can cause numerical difficulties. Furthermore, a range of deformation mechanisms operate in the lithosphere that cannot be simply modeled by diffusion creep. We therefore set the dissipation number, Di to zero for depths less than 325 km.

2.3. Data assimilation

We use progressive assimilation of a thermal and kinematic model of surface plate evolution with continuously closing plates [e.g., *Gurnis et al.*, 2012] at 1 Myr intervals (Fig. 2) [*Seton et al.*, 2012]. The plate motion model is based on a merged moving Indian/Atlantic hotspot reference frame [*O'Neill et al.*, 2005] from 100 Ma and a true polar wander-corrected reference frame [*Steinberger and Torsvik*, 2008] for older ages. The Pacific is anchored to fixed Pacific hotspots prior to 83.5 Ma based on a merged *Wessel et al.* [2006] and *Wessel and Kroenke* [2008] reference frame. The proto-Pacific/Panthalassa evolved from an Izanagi–Farallon–Phoenix triple junction. Importantly, the plate model incorporates the break-up of the Ontong Java–Manihiki–Hikurangi plateaus between 120–86 Ma. The Tethys Ocean is reconstructed largely based on a combination of *Stampfli and Borel* [2002] and *Heine et al.* [2004]. GPlates [*Gurnis et al.*, 2012] exports plate velocities from the digitized plate boundary dataset, providing the kinematic boundary condition on the top surface with linear interpolation between the plate model ages.

The lithosphere in the plate motion model has a net rotation which also drives a net westward drift of the mantle in several of our convection calculations (discussed later). We therefore remove the net rotation of the mantle beneath the lithosphere at each time step because the plate model reference frame should approximately correspond to a mean mantle reference frame with zero net rotation ("RNR", Table 2).

We create a thermal model for the lithosphere using reconstructed seafloor ages and a half-space cooling model (Fig. 3). A thermal age of 200 Ma is assigned to non-oceanic regions. At each time step in the computation, for depths $\leq$ 60 km, the code blends the lithosphere thermal model with the temperature field from the previous time step [see

Matthews et al., 2011, for details]. This approach suppresses convective instabilities away from convergent plate margins and dictates the global surface heat flux.

To construct a thermal slab model we use the paleolocation and age of the oceanic lithosphere at convergent plate margins. We then select a slab dip angle (45° for simplicity) and apply a half-space cooling model on either side of the slab center line to conserve buoyancy. This thermal structure is assimilated at each time step using a blending stencil. The method ensures that slab buoyancy in the upper mantle is consistent with surface plate evolution and allows our simulations to capture the essential aspects of subduction such as asymmetric geometry and slab roll-back. The details are described in *Bower et al.* [2015].

2.4. Parameter space

The height of high-K domes will adjust according to the height of neutral buoyancy (HNB) as dictated by material properties and temperature contrasts [*Tan and Gurnis*, 2005]. To estimate the expected temperature differences we computed a preliminary BO model with the same parameters as BO5 (Table 2). An internal heating rate $H = 100$ accounts for around 60% of the total heat flux. In the preliminary model, the interior temperature of the domes reaches a steady-state temperature of ≈ 2800 K but the ambient material temperature evolves as relatively cold slabs accumulate at the CMB. At 250 Ma (model start time) the ambient material outside of the domes has an average temperature of 1800 K and cools to 1600 K at present day. The assimilation method is not unduly affected by this cooling because the efficient advection of slabs ensures that the upper mantle temperature remains close to the mantle potential temperature which is 1800 K for BO models. Rather, the dominant influence of this temperature change is to increase the

HNB. This basic analysis provides a convenient method to determine the likely evolution of high-K structures without the need for many expensive computations (Table 2).

Tan et al. [2011] generate high-K domes within a spherical geometry with free-convection using density contrasts at the CMB between ≈ 1 and 2%. We anticipate requiring upper values from this range for the domes to remain stable during 250 Myrs of tectonic evolution.

2.5. Initial condition

Precalculations without data assimilation reveal that about 700 Myrs is required for high-K material to develop into high standing structures from an initial layer at the CMB. At the start of our models (250 Ma) we therefore choose to prescribe two domes with a footprint that together occupies 20% of the CMB surface area (Fig. 1b). We explore the influence of the initial condition by exploring two positions for the domes at 250 Ma. First, the domes are positioned at center-of-mass estimates for the LLSVPs inferred from tomography: (13°,-16°) and (197°,-11°) for the African and Pacific structures, respectively [*Burke et al.*, 2008]. Second, the domes are displaced from the present day position of the LLSVPs, with the African structure marginally further north (0°,0°) and the Pacific structure displaced slighly west (180°,0°) (Fig. 4a). For simplicity we define a height of 900 km for the domes and accept that this will adjust to the HNB (Fig. 4d). The total volume of both structures is approximately 34.4×10^9 km^3 which is comparable to the volume of a 200-km-thick layer residing at the CMB. This volume is about a factor of 2 larger than estimates from seismic tomography [*Burke et al.*, 2008; *Hernlund and Houser*, 2008], but comparable to other geodynamic studies [*McNamara and Zhong*, 2005; *Zhang*

et al., 2010]. Additionally, entrainment reduces the size of the structures during the model run.

For EX models, the 3700 K total temperature drop is composed of 1350 K across each boundary layer and an adiabatic temperature increase of 1000 K across the whole mantle (see *Stixrude and Lithgow-Bertelloni* [2011], Fig. 15). The interiors of the structures have a temperature of 3400 K, which is about 900 K hotter than ambient mantle located at the same height above the CMB as the initial vertical center of the structures. Thin thermal boundary layers ($\approx$ 80 km) conduct heat from the top of the domes and the CMB to ambient mantle. For BO models, the temperature drop across the mantle is 3000 K and is equally partitioned between the boundary layers. Ambient mantle is assigned a temperature of 1800 K and the interiors of the structures are 900 K hotter than ambient. These approaches effectively assume that most of the domes existed as two coherent and relatively well-mixed structures prior to the early Mesozoic. The thermal model for the lithosphere and slabs is described in Section 2.3. Slabs are initially inserted from the surface to the base of the transition zone (670 km depth).

3. Results

3.1. Reference model

Fig. 4 illustrates the evolution of our reference model (EX4). The domes initially flatten slightly which increases their CMB footprint (Fig. 4b,e) although they remain largely undeformed until 210 Ma. At 200 Ma, the Pacific dome is indented by western Pacific slabs that produce an embayment along its boundary (e.g., Fig. 4c) and the embayment is gradually enlarged through to present day (Fig. 4i). Meanwhile, from 180 Ma, slabs from Africa-Eurasian collision displace material from North Africa (e.g.,

Fig. 4c). This elongates the African dome north-south in the northern hemisphere and west-east in the southern hemisphere (e.g., Fig. 4g). The domes can develop steep edges from boundary tractions caused by slab-induced flow (for example, the eastern edge of the Pacific anomaly, Fig. 4f, at -95°). Elsewhere the edges are tapered, such as the eastern boundary of the African structure (Fig. 4f, at 65°). The African dome is situated entirely beneath the reconstructed African continent until 120 Ma, after which seafloor spreading in the South Atlantic moves Africa northeastward (Fig. 4h). From 100 Ma, circum-Pacific slabs slightly elongate the Pacific structure north-south.

Fig 5 shows the lower mantle of EX4 at 90 Ma. Descending Tethyan slabs thicken the lower thermal boundary layer and sweep instabilities toward the edge of the African dome (1). This also produces the embayment along the northeastern boundary of the African structure (see also Fig. 4g). Thermal plumes that develop at dome edges can locally elevate the chemical layer (2). Furthermore, thermal plumes of ambient material develop from interconnected ridges of thickened boundary layer located away from the domes (3). Encroaching slabs produce the embayment along the western edge of the Pacific structure (4), and linear ridges of thickening boundary layer at the CMB depict the former geometry of convergent margins at the surface (5). The eastern boundary of the Pacific dome rises high above the CMB even though a slab is not undercutting this edge (6). Rather, the edge instability is presumably caused by the large-scale flow induced by slabs (see also Fig. 4j). Finally, around 170 Ma a thin tendril of chemically distinct material extends away from the African dome and joins with the Pacific structure at 90 Ma (7).

The final position of the African structure is beneath northwest and south Africa, while the Pacific structure is centrally located beneath the Pacific Ocean (Fig. 4i). Circular

embayments punctuate the edge of the domes so both structures have a CMB footprint that resembles an elongated kidney that trends north-south at present day. The high-K structures have steep vertical walls which demonstrates *a posteriori* that the initial thermal and compositional structure for the domes (Fig. 4a,d) is dynamically compatible with the parameters of the calculations. Topography on the top of the domes is slightly concave-up as plumes elevate the edges of the structures whilst the central regions are comparatively depressed.

Our suite of models investigate the influence of the Rayleigh number (Ra), rheology (η_C, η_Z), chemical density profile ($\delta\rho_{ch}$, δK), thermal expansion profile (α), and initial position (at 250 Ma) of the domes (Table 2).

3.2. Stability of high-K structures

The domes in the reference model (EX4) deform readily in response to slabs but have sufficient intrinsic density contrast to remain stable at the CMB ("stable", Table 2). By contrast, some domes are "unstable". EX1 has similar parameters to EX4, but the Ra is increased by a factor of 2 ($Ra = 1.13 \times 10^8$) and the thermal expansion profile is uniform (Fig. 6). The high-K structures are destabilized by their thermal buoyancy and stresses exerted by slabs on their side walls (Fig. 6e). From 160 to 80 Ma, the structures deform substantially and their side walls steepen beyond vertical; ultimately they rise off the CMB (Fig. 6f). In comparison to EX1, a thermal expansion profile that decreases more strongly in the upper mantle than the lower mantle can stabilize the domes (EX2). This profile reduces the effective Rayleigh number with increasing pressure which decreases the thermal buoyancy of the domes and slabs.

BO1 and BO2 have a larger Rayleigh number ($Ra = 1.83 \times 10^8$), a linear thermal expansion profile, and different chemical density profiles, compared to EX1. Furthermore, slabs are stronger in these cases because they have more thermal buoyancy, and are therefore cooler and more viscous at all mantle depths because the transit time through the mantle is reduced ($\sim$ 50 Myr). In BO1, slabs exert large stresses on the side walls of the domes and can slide beneath the high-K structures, further destabilizing them. The African dome rises off the CMB around 140 Ma. In BO2, we increase the density contrast at the CMB ($\delta\rho_{ch} = 2.5\%$) while retaining the same bulk modulus anomaly ($\delta K = 6\%$). In this model, the African structure remains stable at the CMB until about 70 Ma (Fig. 7c,e). BO5 does not include a high-K component and the thermal expansion profile is uniform, yet the evolution of the model from 250 to 70 Ma is similar to BO2 (Figs. 7a,c,e). In comparison to BO2, BO5 achieves both stable domes and less entrainment, although the domes do not stand as high above the CMB and their edges are less steep. This is particularly evident for the African anomaly.

3.3. Parameter variation

In EX5, a reduced Rayleigh number ($Ra = 2.26 \times 10^7$) decreases the sinking rate of slabs because it is equivalent to increasing the background viscosity uniformly compared to the reference model (EX4). Furthermore, the lower-mantle viscosity increases more strongly with pressure. The domes in EX5 stand slightly higher from the CMB, have steeper sides, and flatter tops. They are also less deformed; the distinctive embayments which form in EX4 along the northeastern edge of the African dome and the western boundary of the Pacific structure are absent. Negligible thickening of the lowermost thermal boundary layer precludes plume development and the eastern edge of the Pacific dome is elevated

comparable to EX4 (Fig. 5). The domes are located similarly to EX4 at present day (Fig. 4i), although the Pacific structure is not stretched north-south (Fig. 8c). In EX6, we increase both $\delta\rho_{ch}$ and δK to 2.5% and 6%, respectively, relative to EX5. The domes evolve analogously to EX5 although they flatten and their edges are less steep which increases their CMB footprint (Fig. 8d).

McNamara and Zhong [2004] demonstrate that an intrinsic viscosity increase in the chemically distinct material can control the style of deformation of the domes; rounded, isolated piles are preferred to ridges. In comparison to EX6, the domes in EX7 have a factor 100 intrinsic viscosity increase ($\eta_C = 100$) and the same chemical density profile. The structures in EX7 have steep sides comparable to EX5, which is contrary to the domes that flatten in EX6. Neither dome experiences significant deformation since the initial prescribed geometry is largely retained. At present, the structures are slightly displaced from their initial positions at 250 Ma (Fig. 8e). BO4 also has an intrinsic viscosity increase and qualitatively we observe similar features as EX7. However, the Rayleigh number is larger ($Ra = 1.83 \times 10^8$) and strong slabs are able to undercut the domes which steepens the edges of the structures beyond vertical which produces overhanging walls.

EX3 has the same parameters as the reference model (EX4) but we arbitrarily perturb the position of the domes at the start of the model between 11° and 17°. At 250 Ma, the African and Pacific structures are positioned at the equator at 0° and 180° longitude, respectively. The evolution of this model is similar to EX4 and the location of the domes at present day is almost identical (Fig. 8a,b).

Compared to the EX cases, most BO models have a higher Rayleigh number, a linear thermal expansion profile, do not remove net rotation of the mantle beneath the litho-

sphere, and the domes are initially positioned at (0°,0°) and (180°,0°). In BO5, the domes flatten significantly during the first 20 Myrs which increases their CMB footprint four-fold. This enables Central American slabs to slice a small region from the African structure around 230 Ma and this material migrates southwestward and eventually merges with the Pacific structure at $\sim$ 200 Ma. Additionally, the African dome develops a limb at 200 Ma that extends beneath northwest North America. This extension merges with the northwest boundary of the Pacific dome around 140 Ma, and slabs eventually detach the limb from the main African structure at 100 Ma.

By contrast, the domes in BO6 do not flatten at the start of the model. Nevertheless, Central American slabs carve a portion out of the African structure around 110 Ma which merges with the Pacific dome at $\sim$ 80 Ma as well illustrated by the particle paths (Fig. 8f). This is similar to the behavior in BO5 although the timescale is increased for the lower Ra model. At present, the African structure is elongated north–south and located beneath the Atlantic Ocean with its eastern margin roughly following the western coastline of Africa. Compared to the EX cases, this dome migrates farther to the west in BO models because the mantle beneath the lithosphere is coupled to the net rotation (generally a westward drift) of the plate model. The Pacific structure is stretched west-east and located beneath the Pacific Ocean, although preferentially to the west.

Geodynamic studies often apply a purely kinematic boundary condition to the top surface of models to produce downwellings at convergent plate margins. However, with this approach it is not clear if the downgoing buoyancy flux is reasonable for the convergence rate and lithospheric buoyancy predicted by geologically consistent plate reconstructions. Therefore, we compare the influence of lithosphere and slab assimiliation (BO2) with a

purely kinematic boundary on the top surface (BO3) (Fig. 7); all model parameters are otherwise identical. The assimilation method increases slab flux into the lower mantle and the domes have steeper sides and reduced volume.

4. Discussion

4.1. Evolution of the thermochemical domes

In our preferred models (EX3–7), the domes remain as individual coherent structures from 250 Ma to present and do not exchange mass between each other (Fig. 9). The center of mass of the African dome remains mostly stationary while it extends beneath northern African and the Indian Ocean (Fig. 8). From 250 to 200 Ma, the Paleo-Tethys seafloor is relatively old and introduces a large amount of negative buoyancy into the mantle at the trench through slab assimilation. This is compounded by the Tethyan/Mongol-Okhotsk triple junction (T-T-T) that exists from 250 to 151 Ma (Fig. 2a,b), and slabs descend toward the CMB and push material southwestward toward present day Africa. At present day the African dome resembles an elongated kidney shape that is located within the -0.6% S-wave contour from SB10L18. This ridge-like morphology agrees with waveform modeling [*Ni and Helmberger*, 2003a] and other geodynamic studies [e.g., *McNamara and Zhong*, 2005].

Tomographic inversions suggest that the basic morphology of the Pacific structure is a rounded pile slightly elongated in longitude (Fig. 1). Our Pacific dome is displaced further east ($\approx$ 25 degrees) than tomography suggests, presumably because slabs from the western Pacific subduction zones are dominant in pushing the structure beneath the Pacific Ocean. It is also slightly extended in the latitudinal direction which implies that slabs originating from subduction zones in the north and south Pacific (versus the west

and east margins) are less dominant in shaping the boundaries of the dome. A tabular upwelling elevates the eastern margin of the Pacific structure in our preferred models (Fig. 5, label 6). The reason for this upwelling is uncertain because a slab does not push material towards that margin. Therefore, we expect that the large-scale flow caused by slabs induces this upwelling. Adjusting the initial position of the domes at 250 Ma by ≈ 10 degrees longitude and latitude only marginally influences the evolution and present-day position of the structures (Fig. 8a,b). In BO6 the net rotation of the mantle is not removed and the Pacific structure is generally well located (Fig. 8f); however, the African structure is located too far west (≈ 30 degrees).

At high Rayleigh number (small η_0), downwellings significantly deform the domes (e.g., Fig. 8b). Slabs produce sufficient stresses to generate large embayments along the north-eastern boundary of the African structure and the western edge of the Pacific dome. Furthermore, an active lower thermal boundary layer spawns upwellings at the perimeter of the domes and from ridges between the structures (Fig. 5). Conversely, at low Rayleigh number (large η_0) the domes have less edge deformation and plume activity is reduced. In addition, the structures have high topography and steep sides because stresses are large [*Tackley*, 1998]. Domes with increased intrinsic viscosity (EX7, BO4) do not deform readily in response to slabs, retain a relatively flat top, and become hotter because convection is inhibited [*McNamara and Zhong*, 2004]. A large compositional density anomaly produces flatter domes with more gradational edges and reduced height. However, the lateral motion of the structures is not unduly affected because of the free-slip boundary condition at the CMB.

For BO6 ($Ra = 1.83 \times 10^7$), the shape and areal extent of the domes at 2600 km depth correlate fairly well to tomography (Fig. 8f). The African structure is displaced too far west in all models that do not enforce zero net rotation of the mantle beneath the lithosphere at each timestep. A sliver of the African dome is carved from the main anomaly by slabs from Central American subduction, which eventually merges with the eastern boundary of the Pacific structure (Fig. 8f, leftmost tracer). This demonstrates how mass transfer between the domes [*McNamara et al.*, 2010] may be intimately linked to paleogeography.

4.2. Assimilation and kinematic surface boundary condition

A purely kinematic surface boundary condition (BO3) displaces and deforms the domes similar to a model with comparable parameters with lithosphere and slab assimilation (Fig. 7). However, the assimilation method increases the down flux into the lower mantle, which has two main effects. First, the stronger slab push steepens the boundaries of the domes. Second, the lower mantle is more efficiently cooled, which raises the HNB of the high-K structures. Therefore, with realistic slab fluxes we expect high-K structures to be less stable than the prediction from models with purely kinematic boundary conditions.

Assimilation ensures that the thermal buoyancy contained within the oceanic lithosphere in the plate model is advected coherently into the upper mantle. The thermal structure and geometry of the assimilated slabs is consistent with geological and seismological inferences and a robust and coherent downwelling evolves. Conversely, for a model with a purely kinematic surface boundary condition, slabs advectively thicken at convergent margins and do not produce one-sided subduction. Downwellings in a kinematic model are often manifest as drips with small lengthscale that detach from the top bound-

ary layer. By contrast, assimilated slabs are more voluminous and have more buoyancy which allows them to descend deeper into the mantle. These slabs have a larger lengthscale and therefore a larger diffusion time which allows them to remain as coherent structures near the CMB for longer time. This simple analysis provides the basis for a quantitative assessment of the down flux into the lower mantle for models with assimilation and purely kinematic boundary conditions [see *Bower et al.*, 2015, for details].

4.3. Slab sinking rate and plumes

The slab sinking rate for the models bound a geological estimate of 1.2 cm yr^{-1} [*van der Meer et al.*, 2010]. This is controlled by the Stokes sinking velocity which is proportional to the driving density contrast and inversely proportional to the background viscosity. BO2 (with assimilation) and BO3 (purely kinematic) at 70 Ma have approximately the same age-depth relation (Fig. 10c), despite the significantly increased lower-mantle slab flux from slab assimilation. This is because cooler material in the lower mantle reduces the driving density contrast for subsequent downwellings. Furthermore, the bulk background viscosity increases through the temperature-dependent viscosity, which further reduces the sinking velocity of slabs (Fig. 10a). BO3 actually has a marginally faster sinking rate throughout the lower mantle.

We observe plumes forming at the edges of the domes [*Tan et al.*, 2011; *Steinberger and Torsvik*, 2012] from thickened boundary layer pushed toward the structures by slabs (Fig. 5). However, plume formation is partly controlled by the stability (Rayleigh number) and the maturity (thermal buoyancy available at the CMB) of the lower thermal boundary. Models without preexisting plume conduits in the initial condition are more successful at producing plumes at the margins of the domes [*Steinberger and Torsvik*, 2012]. In

addition, a 250 Myr integration time is not sufficient for a statistical analysis of plume distribution.

4.4. High-K structures

A high-K material for the LLSVPs is inferred from seismic data. Unless the LLSVPs have very low density (≤ -2 %), which is not dynamically plausible, the bulk modulus of its material must be larger than ambient values [*Tan and Gurnis*, 2005]. Furthermore, previous dynamic models with a high-K component can produce stable structures that extend several hundred kilometers above the CMB [e.g., *Tan and Gurnis*, 2005, 2007] in agreement with height estimates from seismic waveform modeling [e.g., *Ritsema et al.*, 1998]. For the high-K structures in most of our models (excluding EX1, BO1), the chemical density anomaly is larger than the thermal density anomaly across the whole mantle pressure range. This prevents slabs from sliding beneath the domes and the structures rising off the CMB. However, a HNB does not exist and the high-K material effectively replicates a high-density layer. Nevertheless, the domes in these models are still elevated substantially above the CMB (up to around 900 km) in accordance with seismic data. Furthermore, they are stable and generally coherent with sharp steep walls, similar to models without slabs [*Tan and Gurnis*, 2005, 2007]. Our models suggest that near-neutrally buoyant domes, such as high-K structures, are unlikely to remain stable at the CMB in the presence of strong slabs.

We consider the density anomaly at the CMB (relative to ambient material) for high-K material, $\Delta\rho_k$, and slab, $\Delta\rho_s$. High-K structures form when $\Delta\rho_k < 0$, and to ensure they remain stable in the presence of slabs requires $\Delta\rho_k > \Delta\rho_s$. However the latter relation cannot be true because $\Delta\rho_s > 0$. Therefore, slabs will always have a tendancy to sweep

beneath high-K structures unless $\Delta\rho_k$ is large and thermal buoyancy no longer dominates at depth. Furthermore, the hot domes have low viscosity and therefore deform readily in response to stresses from stiffer slabs. This further enables slabs to compromise stability by sliding beneath the domes. Higher intrinsic viscosity for the high-K structures can partly mitigate this effect (EX7, BO4).

5. Conclusions

We present models that investigate the stability and morphology of high bulk modulus structures in the lower mantle from 250 Ma to present day with constraints from paleogeography. The African and Pacific structures deform and migrate along the CMB in response to plate motions and slab stresses. Our models produce a ridge-like anomaly beneath Africa and a rounded pile beneath the Pacific Ocean. Strong (fast-sinking) slabs can form prominent embayments along the boundaries of the domes and edge deformation is greatly reduced for a large background viscosity or domes that have an increased intrinsic viscosity contrast. Slabs also thicken the lower thermal boundary layer which forms linear ridges that can spawn plumes at the perimeter of the domes or between the domes. The positions of the structures agrees well with tomography although the Pacific dome is displaced slightly farther east. This eastward drift may result from our plate model and we will test other reconstructions [e.g., *Doubrovine et al.*, 2012] in a future study. Nevertheless, both structures are substantially elevated above the CMB and have steep sides in agreement with seismic observations.

High-K structures rely on a delicate dynamic balance between thermal and chemical buoyancy; they are almost neutrally buoyant because net density differences are small. Therefore, high-K domes are passive components and the flow is largely imposed by plate

motions and slabs. Strong slabs that are more dense and more viscous than the structures generate stresses that can compromise the stability of the domes at the CMB. Additionally, these slabs can further steepen the edges of high-K structures (or uniform dense layers) and may slide beneath the domes, which can cause the structures to raise off the CMB. Relative to models without slabs, the parameter space for stable high-K structures appears to be reduced. Furthermore, even a layer that is more dense than ambient at all mantle pressures (i.e., a height of neutral buoyancy does not exist) can evolve into a structure with steep edges and a high top. Therefore a high-K material for the LLSVPs may not be necessary to satisfy dynamic constraints.

Acknowledgments. We obtained CitcomS version 3.0 from the Computational Infrastructure for Geodynamics (CIG). GPlates is developed at the University of Sydney, California Institute of Technology, and the Geological Survey of Norway (available from http://www.gplates.org). We thank Eh Tan for providing guidance on code modification and useful discussions. Comprehensive and thoughtful reviews from Paul Tackley, Allen McNamara, and Associate Editor Bernhard Steinberger enhanced the manuscript. Most figures in this paper were produced using GMT. DJB and MG acknowledge NSF grants EAR-0855815 and EAR-0810303. MS acknowledges Australian Research Council grant DP0987713.

References

Billen, M. I., and G. Hirth (2007), Rheologic controls on slab dynamics, *Geochem. Geophy. Geosys.*, *8*(8), Q08012, doi:10.1029/2007GC001597.

Bower, D. J., M. Gurnis, and N. Flament (2015), Assimilating lithosphere and slab history in 4-D Earth models, *Phys. Earth Planet. Inter.*, *238*, 8–22, doi: 10.1016/j.pepi.2014.10.013.

Burke, K., and T. H. Torsvik (2004), Derivation of large igneous provinces of the past 200 million years from long-term heterogeneities in the deep mantle, *Earth Planet. Sci. Lett.*, *227*(c), 531–538, doi:10.1016/j.epsl.2004.09.015.

Burke, K., B. Steinberger, T. H. Torsvik, and M. A. Smethurst (2008), Plume generation zones at the margins of large low shear velocity provinces on the core-mantle boundary, *Earth Planet. Sci. Lett.*, *265*, 49–60, doi:10.1016/j.epsl.2007.09.042.

Davaille, A., F. Girard, and M. Le Bars (2002), How to anchor hotspots in a convecting mantle?, *Earth Planet. Sci. Lett.*, *203*(2), 621–634, doi:10.1016/S0012-821X(02)00897-X.

Davies, D. R., and J. H. Davies (2009), Thermally-driven mantle plumes reconcile multiple hot-spot observations, *Earth Planet. Sci. Lett.*, *278*(1–2), 50–54, doi: 10.1016/j.epsl.2008.11.027.

Deschamps, F., and P. J. Tackley (2008), Searching for models of thermo-chemical convection that explain probabilistic tomography: I. Principles and influence of rheological parameters, *Phys. Earth Planet. Inter.*, *171*(1–4), 357–373, doi: 10.1016/j.pepi.2008.04.016.

Doubrovine, P. V., B. Steinberger, and T. H. Torsvik (2012), Absolute plate motions in a reference frame defined by moving hot spots in the Pacific, Atlantic, and Indian oceans, *J. Geophys. Res.*, *117*(B9), B09101, doi:10.1029/2011JB009072.

Grand, S. P. (2002), Mantle shear-wave tomography and the fate of subducted slabs, *Phil. Trans. R. Soc. Lond. A*, *360*(1800), 2475–2491, doi:10.1098/rsta.2002.1077.

Gurnis, M., et al. (2012), Plate tectonic reconstructions with continuously closing plates, *Comput. Geosci.*, *38*, 35–42, doi:10.1016/j.cageo.2011.04.014.

He, Y., and L. Wen (2009), Structural features and shear-velocity structure of the "Pacific Anomaly", *J. Geophys. Res.*, *114*, B02309, doi:10.1029/2008JB005814.

He, Y., L. Wen, and T. Zheng (2006), Geographic boundary and shear wave velocity structure of the "Pacific anomaly" near the core-mantle boundary beneath western Pacific, *Earth Planet. Sci. Lett.*, *244*, 302–314, doi:10.1016/j.epsl.2006.02.007.

Heine, C., R. D. Müller, and C. Gaina (2004), Reconstructing the lost eastern Tethys Ocean basin: Constraints for the convergence history of the SE Asian margin and marine gateways, in *Continent--Ocean Interactions within East Asian Marginal Seas*, *Geophys. Monogr. Ser.*, vol. 149, edited by P. Clift, P. Wang, W. Kuhnt, and D. Hayes, pp. 37–54, AGU, Washington, D.C., doi:10.1029/GM149.

Helmberger, D., S. Ni, L. Wen, and J. Ritsema (2000), Seismic evidence for ultralow-velocity zones beneath Africa and the eastern Atlantic, *J. Geophys. Res.*, *105*(B10), 23,865–23,878, doi:10.1029/2000JB900143.

Helmberger, D. V., and S. Ni (2005), Seismic modeling constraints on the South African super plume, in *Earth's Deep Mantle: Structure, Composition, Evolution*, *Geophys. Monogr. Ser.*, vol. 160, edited by R. D. van der Hilst, J. D. Bass, J. Matas, and J. Trampert, pp. 63–81, AGU, Washington, D.C., doi:10.1029/160GM06.

Hernlund, J. W., and C. Houser (2008), On the statistical distribution of seismic velocities in Earth's deep mantle, *Earth Planet. Sci. Lett.*, *265*, 423–437, doi:

10.1016/j.epsl.2007.10.042.

Ishii, M., and J. Tromp (1999), Normal-mode and free-air gravity constraints on lateral variations in velocity and density of Earth's mantle, *Science*, *285*, 1231–1236, doi: 10.1126/science.285.5431.1231.

Ishii, M., and J. Tromp (2004), Constraining large-scale mantle heterogeneity using mantle and inner-core sensitive normal modes, *Phys. Earth Planet. Inter.*, *146*(1–2), 113–124, doi:10.1016/j.pepi.2003.06.012.

Ita, J., and S. D. King (1994), Sensitivity of convection with an endothermic phase change to the form of the governing equations, initial conditions, boundary conditions, and equation of state, *J. Geophys. Res.*, *99*(B8), 15,919–15,938, doi:10.1029/94JB00852.

Jellinek, A. M., and M. Manga (2002), The influence of a chemical boundary layer on the fixity, spacing and lifetime of mantle plumes, *Nature*, *418*, 760–763, doi: 10.1038/nature00979.

Karato, S.-I., and P. Li (1992), Diffusion creep in perovskite: Implications for the rheology of the lower mantle, *Science*, *255*(5049), 1238–1240, doi:10.1126/science.255.5049.1238.

Katsura, T., et al. (2009), P-V-T relations of the $MgSiO_3$ perovskite determined by in situ X-ray diffraction using a large-volume high-pressure apparatus, *Geophys. Res. Lett.*, *36*(1), L01305, doi:10.1029/2008GL035658.

Lithgow-Bertelloni, C., and M. Richards (1998), Dynamics of Cenozoic and Mesozoic plate motions, *Rev. Geophys.*, *36*, 27–78, doi:10.1029/97RG02282.

Liu, L., Y. Tan, D. Sun, M. Chen, and D. Helmberger (2011), Trans-Pacific whole mantle structure, *J. Geophys. Res.*, *116*(B4), B04306, doi:10.1029/2010JB007907.

Masters, G., G. Laske, H. Bolton, and A. Dziewonski (2000), The relative behaviour of shear velocity, bulk sound speed, and compressional velocity in the mantle: Implications for chemical and thermal structure, in *Earth's Deep Interior: Mineral Physics and Tomography From the Atomic to the Global Scale*, *Geophys. Monogr. Ser.*, vol. 117, edited by S. Karato, A. M. Forte, R. C. Liebermann, G. Masters, and L. Stixude, pp. 63–87, AGU, Washington, D.C., doi:10.1029/GM117.

Matthews, K. J., A. J. Hale, M. Gurnis, R. D. Müller, and L. DiCaprio (2011), Dynamic subsidence of Eastern Australia during the Cretaceous, *Gondwana Res.*, *19*, 372–383, doi:10.1016/j.gr.2010.06.006.

McNamara, A. K., and S. Zhong (2004), Thermochemical structures within a spherical mantle: Superplumes or piles?, *J. Geophys. Res.*, *109*, B07402, doi: 10.1029/2003JB002847.

McNamara, A. K., and S. Zhong (2005), Thermochemical structures beneath Africa and the Pacific Ocean, *Nature*, *437*, doi:10.1038/nature04066.

McNamara, A. K., E. J. Garnero, and S. Rost (2010), Tracking deep mantle reservoirs with ultra-low velocity zones, *Earth Planet. Sci. Lett.*, *299*(1–2), 1–9, doi: 10.1016/j.epsl.2010.07.042.

Mosenfelder, J. L., P. D. Asimow, D. J. Frost, D. C. Rubie, and T. J. Ahrens (2009), The MgSiO3 system at high pressure: Thermodynamic properties of perovskite, post-perovskite, and melt from global inversion of shock and static compression data, *J. Geophys. Res. Solid Earth*, *114*(B1), doi:10.1029/2008JB005900, b01203.

Ni, S., and D. V. Helmberger (2001a), Probing an ultra-low velocity zone at the core mantle boundary with P and S waves, *Geophys. Res. Lett.*, *28*(12), 2345–2348, doi:

10.1029/2000GL012766.

Ni, S., and D. V. Helmberger (2001b), Horizontal transition from fast to slow structures at the core-mantle boundary; South Atlantic, *Earth Planet. Sci. Lett.*, *187*(3–4), 301–310, doi:10.1016/S0012-821X(01)00273-4.

Ni, S., and D. V. Helmberger (2003a), Ridge-like lower mantle structure beneath South Africa, *J. Geophys. Res.*, *108*(B2), 2094, doi:10.1029/2001JB001545.

Ni, S., and D. V. Helmberger (2003b), Further constraints on the African superplume structure, *Phys. Earth Planet. Inter.*, *140*, 243–251, doi:10.1016/j.pepi.2003.07.011.

Ni, S., and D. V. Helmberger (2003c), Seismological constraints on the South African superplume; could be the oldest distinct structure on Earth, *Earth Planet. Sci. Lett.*, *206*, 119–131, doi:10.1016/S0012-821X(02)01072-5.

Ni, S., X. Ding, D. V. Helmberger, and M. Gurnis (1999), Low-velocity structure beneath Africa from forward modeling, *Earth Planet. Sci. Lett.*, *170*(4), 497–507, doi:10.1016/S0012-821X(99)00121-1.

Ni, S., E. Tan, M. Gurnis, and D. V. Helmberger (2002), Sharp sides to the African superplume, *Science*, *296*, 1850–1852, doi:10.1126/science.1070698.

Ni, S., D. V. Helmberger, and J. Tromp (2005), Three-dimensional structure of the African superplume from waveform modelling, *Geophys. J. Int.*, *161*, 283–294, doi:10.1111/j.1365-246X.2005.02508.x.

Oldham, D., and J. H. Davies (2004), Numerical investigation of layered convection in a three-dimensional shell with application to planetary mantles, *Geochem. Geophy. Geosys.*, *5*(12), Q12C04, doi:10.1029/2003GC000603.

Olson, P., and C. Kincaid (1991), Experiments on the interaction on thermal convection and compositional layering at the base of the mantle, *J. Geophys. Res.*, *96*(B3), 4347–4354.

O'Neill, C., R. D. Müller, and B. Steinberger (2005), On the uncertainties in hot spot reconstructions and the significance of moving hot spot reference frames, *Geochem. Geophy. Geosys.*, *6*, Q04003, doi:10.1029/2004GC000784.

Ritsema, J., S. Ni, D. V. Helmberger, and H. P. Crotwell (1998), Evidence for strong shear velocity reductions and velocity gradients in the lower mantle beneath Africa, *Geophys. Res. Lett.*, *25*(23), 4245–4248, doi:10.1029/1998GL900127.

Ritsema, J., H. J. van Heijst, and J. H. Woodhouse (1999), Complex shear wave velocity structure imaged beneath Africa and Iceland, *Science*, *286*, 1925–1928, doi:10.1126/science.286.5446.1925.

Ritsema, J., A. Deuss, H. J. van Heijst, and J. H. Woodhouse (2011), S40RTS: a degree-40 shear-velocity model for the mantle from new Rayleigh wave dispersion, teleseismic traveltime and normal-mode splitting function measurements, *Geophys. J. Int.*, *184*(3), 1223–1236, doi:10.1111/j.1365-246X.2010.04884.x.

Schubert, G., G. Masters, P. Olson, and P. Tackley (2004), Superplumes or plume clusters?, *Phys. Earth Planet. Inter.*, *146*, 147–162, doi:10.1016/j.pepi.2003.09.025.

Schuberth, B. S. A., H.-P. Bunge, and J. Ritsema (2009), Tomographic filtering of high-resolution mantle circulation models: Can seismic heterogeneity be explained by temperature alone?, *Geochem. Geophy. Geosys.*, *10*(5), Q05W03, doi:10.1029/2009GC002401.

Schuberth, B. S. A., C. Zaroli, , and G. Nolet (2012), Synthetic seismograms for a synthetic Earth: long-period P- and S-wave traveltime variations can be explained by temperature alone, *Geophys. J. Int.*, *188*, 1393–1412, doi:10.1111/j.1365-246X.2011.05333.x.

Seton, M., et al. (2012), Global continental and ocean basin reconstructions since 200 Ma, *Earth Sci. Rev.*, *113*(3–4), 212–270, doi:10.1016/j.earscirev.2012.03.002.

Simmons, N. A., and S. P. Grand (2002), Partial melting in the deepest mantle, *Geophys. Res. Lett.*, *29*(11), 1552, doi:10.1029/2001GL013716.

Simmons, N. A., A. M. Forte, and S. P. Grand (2009), Joint seismic, geodynamic and mineral physical constraints on three-dimensional mantle heterogeneity: Implications for the relative importance of thermal versus compositional heterogeneity, *Geophys. J. Int.*, *177*(3), 1284–1304, doi:10.1111/j.1365-246X.2009.04133.x.

Stacey, F. D. (1977), A thermal model of the Earth, *Phys. Earth Planet. Inter.*, *15*(4), 341–348, doi:10.1016/0031-9201(77)90096-6.

Stadler, G., M. Gurnis, C. Burstedde, L. C. Wilcox, L. Alisic, and O. Ghattas (2010), The dynamics of plate tectonics and mantle flow: from local to global scales, *Science*, *329*, 1033–1038, doi:10.1126/science.1191223.

Stampfli, G., and G. Borel (2002), A plate tectonic model for the Paleozoic and Mesozoic constrained by dynamic plate boundaries and restored synthetic oceanic isochrons, *Earth Planet. Sci. Lett.*, *196*(1–2), 17–33, doi:10.1016/S0012-821X(01)00588-X.

Steinberger, B., and T. H. Torsvik (2008), Absolute plate motions and true polar wander in the absence of hotspot tracks, *Nature*, *452*(7187), 620–623, doi:10.1038/nature06824.

Steinberger, B., and T. H. Torsvik (2010), Toward an explanation for the present and past locations of the poles, *Geochem. Geophy. Geosys.*, *11*(6), Q06W06, doi:

10.1029/2009GC002889.

Steinberger, B., and T. H. Torsvik (2012), A geodynamic model of plumes from the margins of Large Low Shear Velocity Provinces, *Geochem. Geophy. Geosys.*, *13*(1), Q01W09, doi:10.1029/2011GC003808.

Stixrude, L., and C. Lithgow-Bertelloni (2011), Thermodynamics of mantle minerals - II. Phase equilibria, *Geophys. J. Int.*, *184*(3), 1180–1213, doi:10.1111/j.1365-246X.2010.04890.x.

Su, W.-J., and A. M. Dziewonski (1997), Simultaneous inversion for 3-D variations in shear and bulk velocity in the mantle, *Phys. Earth Planet. Inter.*, *100*(1–4), 35–156, doi:10.1016/S0031-9201(96)03236-0.

Sun, D., E. Tan, D. Helmberger, and M. Gurnis (2007), Seismological support for the metastable superplume model, sharp features, and phase changes within the lower mantle, *P. Natl. Acad. Sci. USA*, *104*(22), 9151–9155, doi:10.1073/pnas.0608160104.

Sun, D., D. Helmberger, S. Ni, and D. Bower (2009), Direct measures of lateral velocity variation in the deep Earth, *J. Geophys. Res.*, *114*, B05303, doi:10.1029/2008JB005873.

Sun, D., D. Helmberger, and M. Gurnis (2010), A narrow, mid-mantle plume below southern Africa, *Geophys. Res. Lett.*, *37*(9), L09302, doi:10.1029/2009GL042339.

Tackley, P. J. (1998), Three-dimensional simulations of mantle convection with a thermochemical basal boundary layer: D″?, in *The Core-Mantle Boundary Region*, *Geodyn. Ser.*, vol. 28, edited by M. Gurnis, M. Wysession, E. Knittle, and B. A. Buffett, pp. 231–254, AGU, Washington, D.C., doi:10.1029/GD028.

Tackley, P. J. (2002), Strong heterogeneity caused by deep mantle layering, *Geochem. Geophy. Geosys.*, *3*(4), doi:10.1029/2001GC000167.

Tackley, P. J., and S. King (2003), Testing the tracer ratio method for modeling active compositional fields in mantle convection simulations, *Geochem. Geophy. Geosys.*, *4*(4), 8302, doi:10.1029/2001GC000214.

Takeuchi, N., Y. Morita, N. D. Xuyen, and N. Q. Zung (2008), Extent of the low-velocity region in the lowermost mantle beneath the western Pacific detected by the Vietnamese broadband seismograph array, *Geophys. Res. Lett.*, *35*(5), L05307, doi: 10.1029/2008GL033197.

Tan, E., and M. Gurnis (2005), Metastable superplumes and mantle compressibility, *Geophys. Res. Lett.*, *32*, L20307, doi:10.1029/2005GL024190.

Tan, E., and M. Gurnis (2007), Compressible thermochemical convection and application to lower mantle structures, *J. Geophys. Res.*, *112*, B06304, doi:10.1029/2006JB004505.

Tan, E., W. Leng, S. Zhong, and M. Gurnis (2011), On the location of plumes and lateral movement of thermo-chemical structures with high bulk modulus in the 3-D compressible mantle, *Geochem. Geophy. Geosys.*, *12*(7), Q07005, doi:10.1029/2011GC003665.

Thorne, M. S., and E. J. Garnero (2004), Inferences on ultralow-velocity zone structure from a global analysis of SPdKS waves, *J. Geophys. Res.*, *109*, B08301, doi: 10.1029/2004JB003010.

To, A., B. A. Romanowicz, Y. Capdeville, and N. Takeuchi (2005), 3D effects of sharp boundaries at the borders of the African and Pacific Superplumes: Observation and modeling, *Earth Planet. Sci. Lett.*, *233*, 137–153, doi:10.1016/j.epsl.2005.01.037.

Torsvik, T. H., K. Burke, B. Steinberger, S. J. Webb, and L. D. Ashwal (2010), Diamonds sampled by plumes from the core-mantle boundary, *Nature*, *466*, doi: 10.1038/nature09216.

van der Meer, D. G., W. Spakman, D. J. J. van Hinsbergen, M. L. Amaru, and T. H. Torsvik (2010), Towards absolute plate motions constrained by lower-mantle slab remnants, *Nat. Geosci.*, *3*, 36–40, doi:10.1038/ngeo708.

Wang, Y., and L. Wen (2004), Mapping the geometry and geographic distribution of a very low velocity province at the base of the Earth's mantle, *J. Geophys. Res.*, *109*, B10305, doi:10.1029/2003JB002674.

Wang, Y., and L. Wen (2007a), Geometry and P and S velocity structure of the "African Anomaly", *J. Geophys. Res.*, *112*, B05313, doi:10.1029/2006JB004483.

Wang, Y., and L. Wen (2007b), Complex seismic anisotropy at the border of a very low velocity province at the base of the Earth's mantle, *J. Geophys. Res.*, *112*, B09305, doi:10.1029/2006JB004719.

Wen, L. (2000), Intense seismic scattering near the Earth's core-mantle boundary beneath the Comoros hotspot, *Geophys. Res. Lett.*, *27*(22), 3627–3630, doi:10.1029/2000GL011831.

Wen, L. (2001), Seismic evidence for a rapidly varying compositional anomaly at the base of the Earth's mantle beneath the Indian Ocean, *Earth Planet. Sci. Lett.*, *194*(1–2), 83–95, doi:10.1016/S0012-821X(01)00550-7.

Wen, L. (2002), An SH hybrid method and shear velocity structures in the lowermost mantle beneath the Central Pacific and South Atlantic Oceans, *J. Geophys. Res.*, *107*(B3), doi:10.1029/2001JB000499.

Wen, L. (2006), A compositional anomaly at the Earth's core-mantle boundary as an anchor to the relatively slowly moving surface hotspots and as as source to the DUPAL anomaly, *Earth Planet. Sci. Lett.*, *246*, 138–148, doi:10.1016/j.epsl.2006.04.024.

Wen, L., P. Silver, D. James, and R. Kuehnel (2001), Seismic evidence for a thermo-chemical boundary at the base of the Earth's mantle, *Earth Planet. Sci. Lett.*, *189*, 141–153, doi:10.1016/S0012-821X(01)00365-X.

Wessel, P., and L. W. Kroenke (2008), Pacific absolute plate motion since 145 Ma: An assessment of the fixed hot spot hypothesis, *J. Geophys. Res.*, *113*(B6), B06101, doi: 10.1029/2007JB005499.

Wessel, P., Y. Harada, and L. W. Kroenke (2006), Toward a self-consistent, high-resolution absolute plate motion model for the Pacific, *Geochem. Geophy. Geosys.*, *7*(3), Q03L12, doi:10.1029/2005GC001000.

Zhang, N., S. Zhong, W. Leng, and Z.-X. Li (2010), A model for the evolution of the Earth's mantle structure since the early Paleozoic, *J. Geophys. Res.*, *115*, B06401, doi: 10.1029/2009JB006896.

Zhong, S., M. Zuber, L. N. Moresi, and M. Gurnis (2000), Role of temperature-dependent viscosity and surface plates in spherical shell models of mantle convection, *J. Geophys. Res.*, *105*(B5), 11,063–11,082, doi:10.1029/2000JB900003.

Zhong, S., N. Zhang, Z.-X. Li, and J. H. Roberts (2007), Supercontinent cycles, true polar wander, and very long-wavelength mantle convection, *Earth Planet. Sci. Lett.*, *261*, 551–564, doi:10.1016/j.epsl.2007.07.049.

Zhong, S., A. McNamara, E. Tan, L. Moresi, and M. Gurnis (2008), A benchmark study on mantle convection in a 3-D spherical shell using CitcomS, doi:10.1029/2008GC002048.

Table 1. Generic model parameters

Parameter	Symbol	Value	Units
Dissipation number	Di	1.74 or 0	-
Density	ρ_0	3930	kg m^{-3}
Thermal expansion coefficient	α_0	3×10^{-5}	K^{-1}
Earth radius	R_0	6371	km
CMB radius	$R_{\rm cmb}$	3505	km
Gravity	g_0	10	m s^{-2}
Thermal diffusivity	κ_0	10^{-6}	m^2 s^{-1}
Heat capacity	c_{p0}	1100	J kg^{-1} K^{-1}
Activation energy (Eq. 6)	E	172	kJ mol^{-1}
Surface temperature	T_S	300	K
Heating rate	H	3.2×10^{-8}	W m^{-3}
Grüneisen parameter	γ	2.3	-
Temperature drop	ΔT	3700 or 3000	K

Table 2. Model-specific parameters. [a] Initial position (at 250 Ma) of the African and Pacific structures, respectively [see *Burke et al.*, 2008, Table 1]. [b] Remove net rotation of the mantle beneath the lithosphere. [c] This calculation assumes the domes are 1000 K hotter than ambient material, which is appropriate for the start of the model but evolves as slabs cool the mantle. [d] Unstable: domes rise off CMB. [e] Kinematic boundary condition only (no lithosphere or slab assimilation).

Model	Input									Output	
	Ra	η_0 (Pa s)	η_C	η_Z	$\delta\rho_{ch}$ (%)	δK (%)	Dome Pos. (lon, lat)[a]	α	RNR[b]	HNB (km)[c]	Domes[d]
EX1	1.13×10^8	1×10^{22}	0	6.8	1.7	4	(0°,0°), (180°,0°)	uniform	N	700	unstable
EX2	1.13×10^8	1×10^{22}	0	6.8	1.7	4	(0°,0°), (180°,0°)	M09	N	-	stable
EX3	5.65×10^7	2×10^{22}	0	6.8	1.7	4	(0°,0°), (180°,0°)	M09	Y	-	stable
EX4	5.65×10^7	2×10^{22}	0	6.8	1.7	4	(13°,-16°), (197°,-11°)	M09	Y	-	stable
EX5	2.26×10^7	5×10^{22}	0	12	1.7	4	(13°,-16°), (197°,-11°)	M09	Y	-	stable
EX6	2.26×10^7	5×10^{22}	0	12	2.5	6	(13°,-16°), (197°,-11°)	M09	Y	-	stable
EX7	2.26×10^7	5×10^{22}	100	12	2.5	6	(13°,-16°), (197°,-11°)	M09	Y	-	stable
BO1	1.83×10^8	5×10^{21}	0	6.8	1.8	6	(0°,0°), (180°,0°)	linear	N	700	unstable
BO2	1.83×10^8	5×10^{21}	0	6.8	2.5	6	(0°,0°), (180°,0°)	linear	N	-	unstable
BO3[e]	1.83×10^8	5×10^{21}	0	6.8	2.5	6	(0°,0°), (180°,0°)	linear	N	-	stable
BO4	1.83×10^8	5×10^{21}	100	6.8	2.5	6	(0°,0°), (180°,0°)	linear	N	-	stable
BO5	1.83×10^8	5×10^{21}	0	6.8	$B = 0.5$		(0°,0°), (180°,0°)	uniform	N	-	stable
BO6	1.83×10^7	5×10^{22}	0	6.8	2.5	6	(0°,0°), (180°,0°)	linear	N	-	stable
BO7	6.10×10^7	1.5×10^{22}	0	6.8	2.5	6	(0°,0°), (180°,0°)	linear	N	-	stable

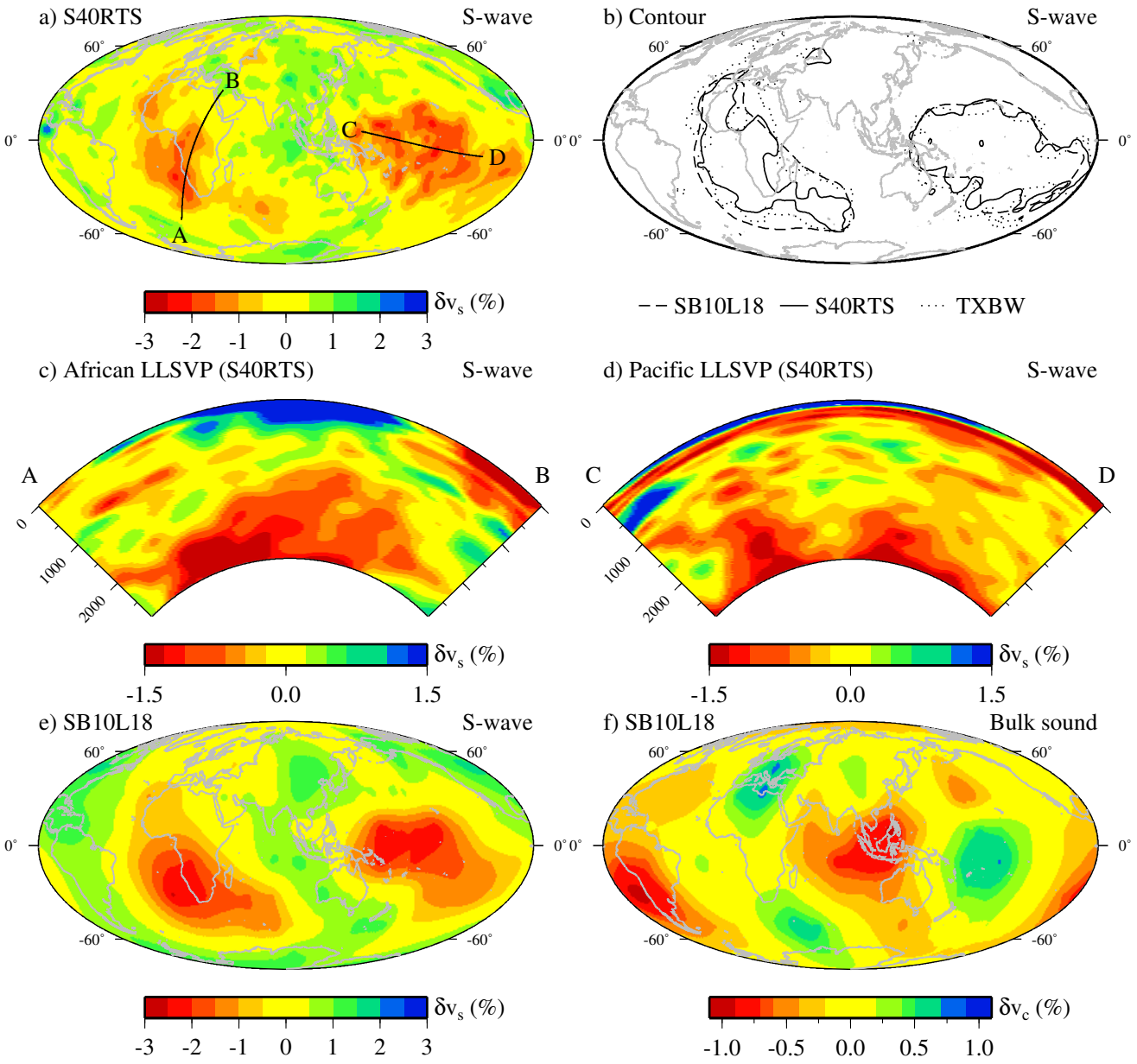

Figure 1. Seismic tomography data for the LLSVPs. (a, e) Shear velocity tomography models at 2800 km depth. (a) S40RTS [*Ritsema et al.*, 2011], (e) SB10L18 [*Masters et al.*, 2000]. (b) -0.6% shear velocity contours from several S-wave tomography models (SB10L18, S40RTS, TXBW [*Grand*, 2002]) at 2800 km depth show their consistency. (c, d) Cross section through the African and Pacific LLSVPs, respectively. The color scale is saturated to highlight mid-mantle structure. Location of cross sections are marked on (a). (f) Bulk sound speed from SB10L18 [*Masters et al.*, 2000] at 2800 km depth. Note approximate anticorrelation with shear velocity in (e).

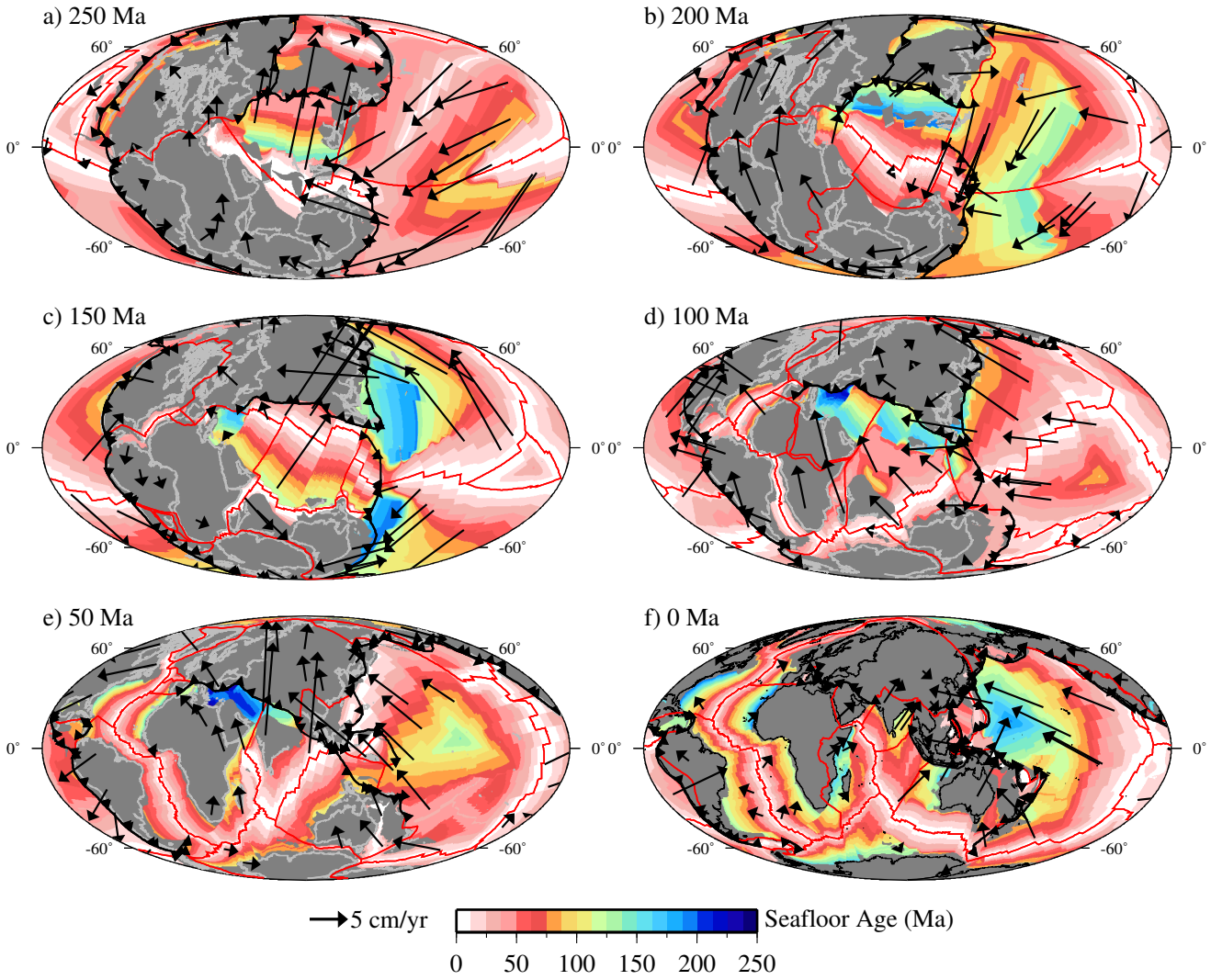

Figure 2. Snapshots of the plate tectonic reconstruction extended from *Seton et al.* [2012] (a) 250 Ma, (b) 200 Ma, (c) 150 Ma, (d) 100 Ma, (e) 50 Ma, (f) present day. Ridges and transform faults are represented by red lines and subduction zones are represented by black lines with sawteeth indicating polarity. Non-oceanic regions are dark grey and reconstructed continents with present-day shorelines are shown in light grey (except black for the present day).

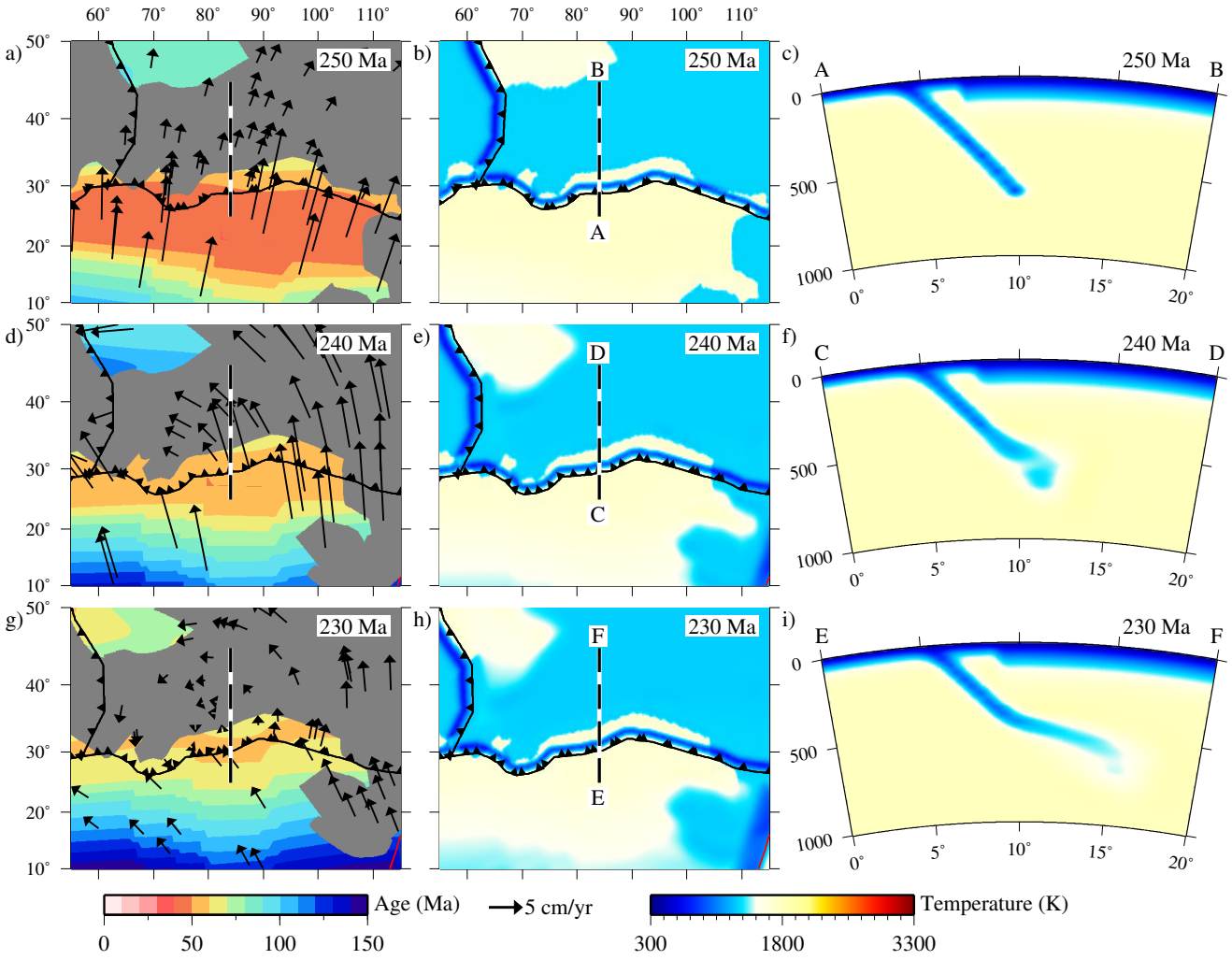

Figure 3. Progressive data assimilation example for the convergence of the Paleo-Tethys Ocean and Laurussia (Model BO6). Plate history and age of oceanic lithosphere model (a) 250 Ma, (d) 240 Ma, (g) 230 Ma. Temperature field at 110 km depth (b) 250 Ma, (e) 240 Ma, (h) 230 Ma. Cross section of slab (c) profile A–B, 250 Ma, (f) profile C–D, 240 Ma, (i) profile E–F, 230 Ma. Ridges and transform faults are represented by red lines and subduction zones are represented by black lines with sawteeth indicating polarity. Non-oceanic regions are dark grey.

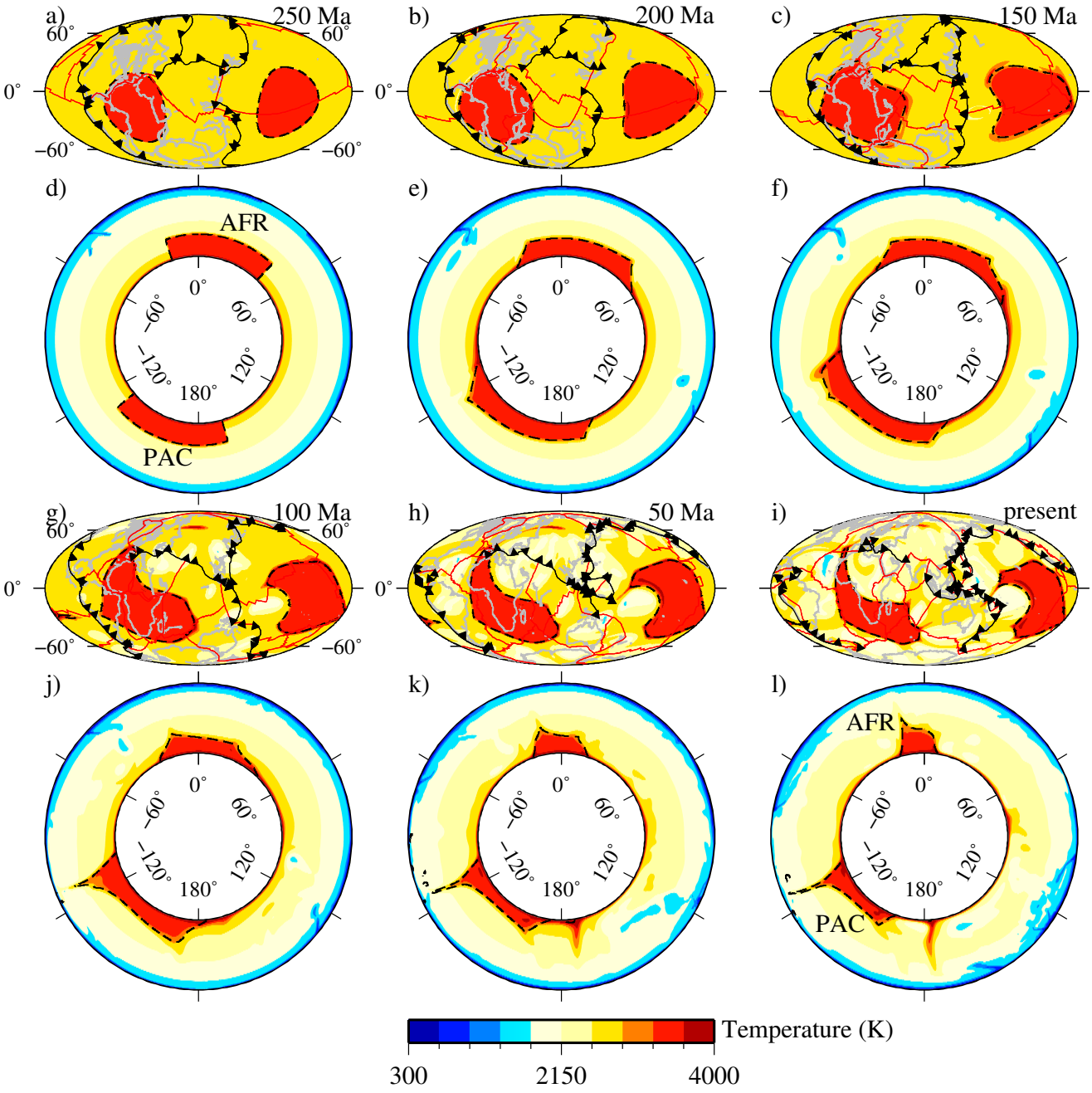

Figure 4. Reference model (EX4) snapshots. (a, b, c, g, h, i) Temperature at 2600 km depth for 250, 200, 150, 100, 50 Ma and present day, respectively. The compositionally distinct material is contoured with black dashed lines. Ridges and transform faults are represented by red lines and subduction zones are represented by black lines with sawteeth indicating polarity. Reconstructed continent outlines are shown in light grey. (d, e, f, j, k, l) Equatorial annuli of temperature (0° is the Prime Meridian) for (a, b, c, g, h, i), respectively. "AFR" and "PAC" identify the domes.

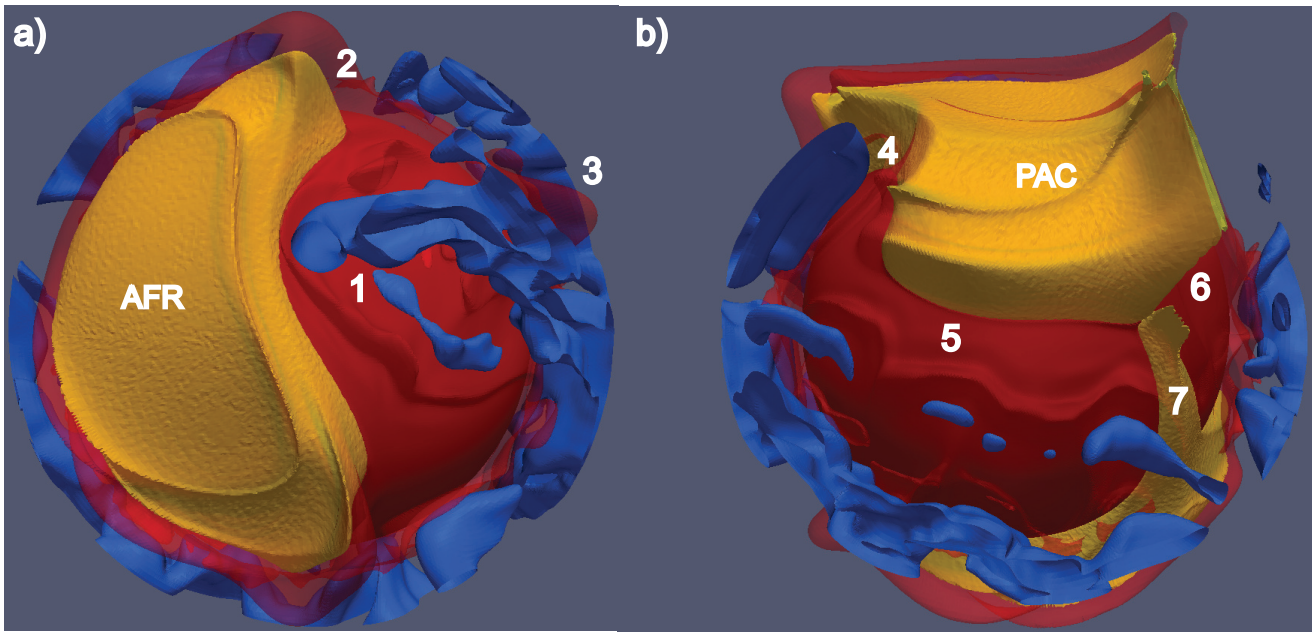

Figure 5. 3-D view of the domes, plumes, and slabs at 90 Ma (Model EX4). The 2500 K isosurface is colored red and is transparent so that the (a) African ("AFR") and (b) Pacific ("PAC") domes (colored yellow) are visible on the CMB. Slabs are colored blue and the upper thermal boundary layer has been removed for clarity. See text for discussion of the labeled regions (1–7).

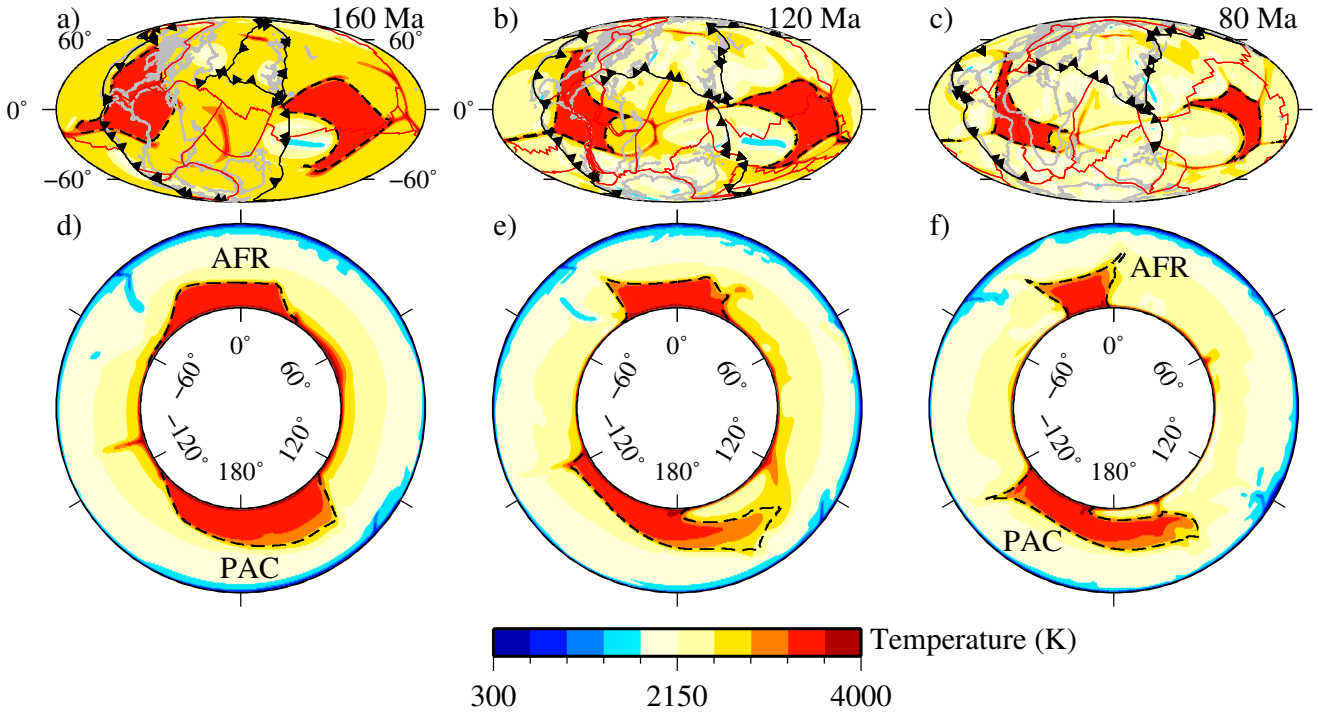

Figure 6. Model EX1 snapshots. (a, b, c) Temperature at 2600 km depth for 160, 120, 80 Ma, respectively. (d, e, f) Equatorial annuli of temperature (0° is the Prime Meridian) for (a, b, c), respectively. For details, see Fig. 4 caption.

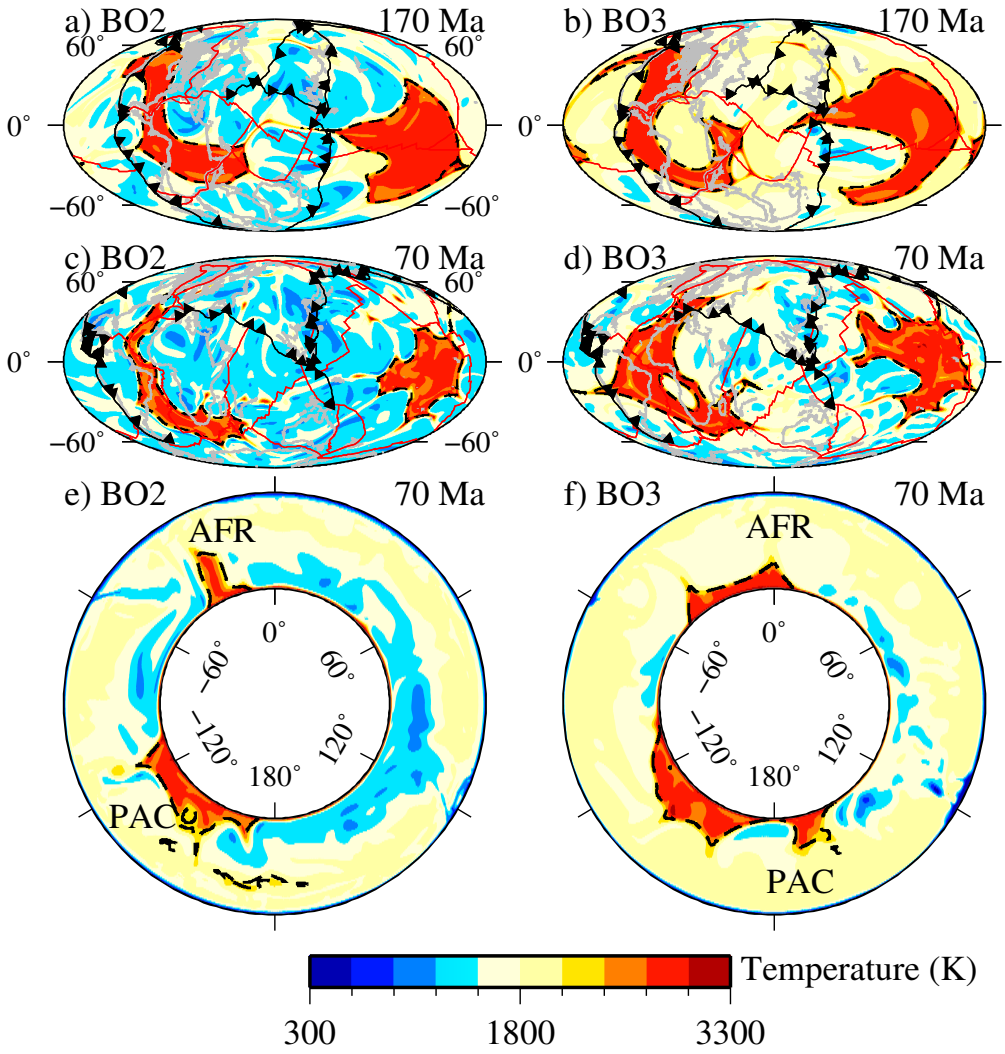

Figure 7. BO2 (with assimilation) and BO3 (kinematic only) snapshots. Temperature at 2600 km depth for (a, c) BO2 at 170 and 70 Ma, respectively. (b, d) BO3 at 170 and 70, respectively. (e, f) Equatorial annuli of temperature (0° is the Prime Meridian) for (c, d), respectively. For details, see Fig. 4 caption.

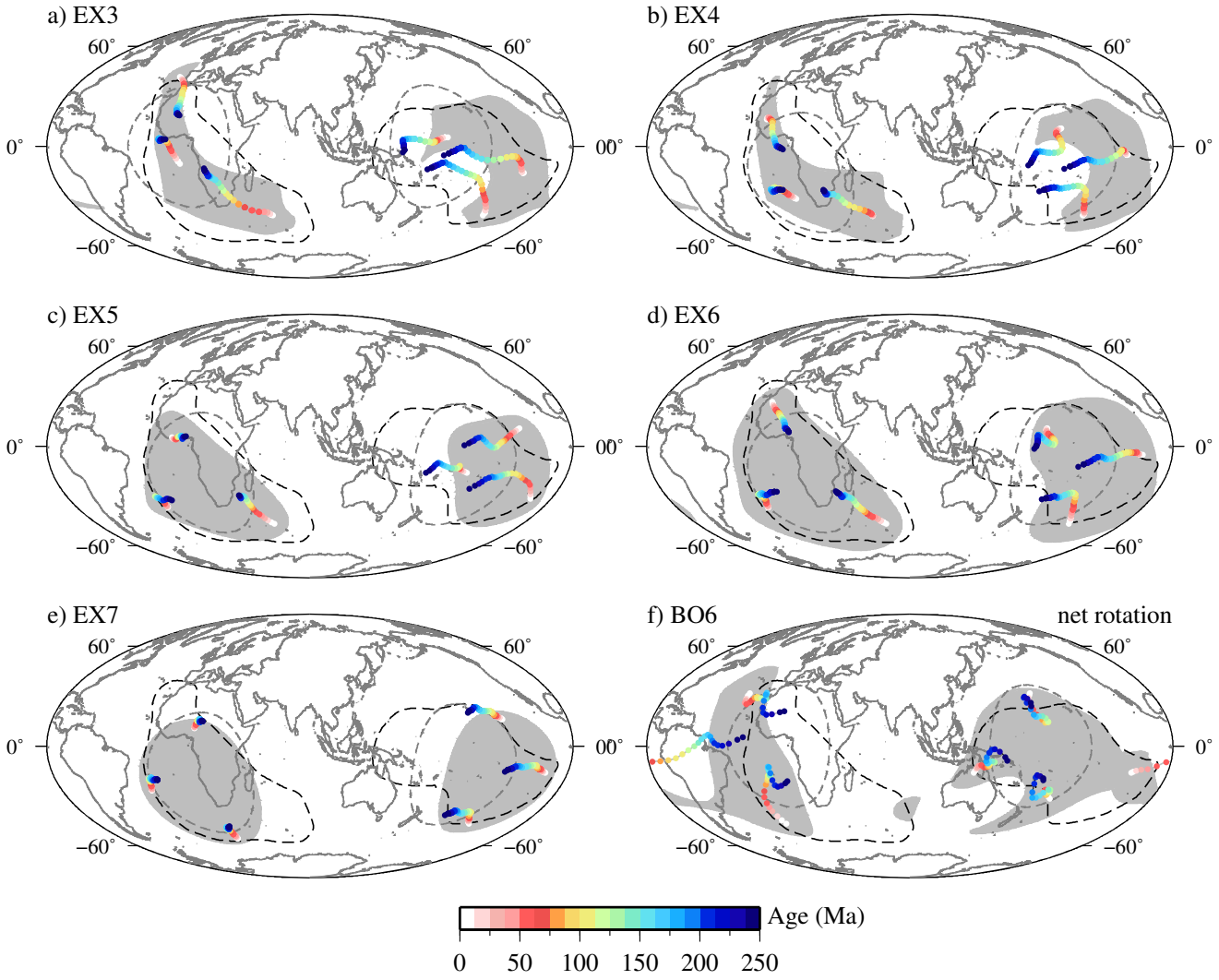

Figure 8. Motion and deformation of the domes at 2600 km depth, (a) EX3, (b) EX4, (c) EX5, (d) EX6, (e) EX7, (f) BO6. The grey-shaded region shows the domes at present day and the grey dashes contour the initial position of the domes at 250 Ma. Black dashes delineate the -0.6% S-wave contour from SB10L18 and continent outlines are shown in solid dark grey. Color-coded dots track the movement of points located within the domes at the CMB from 250 Ma to present day.

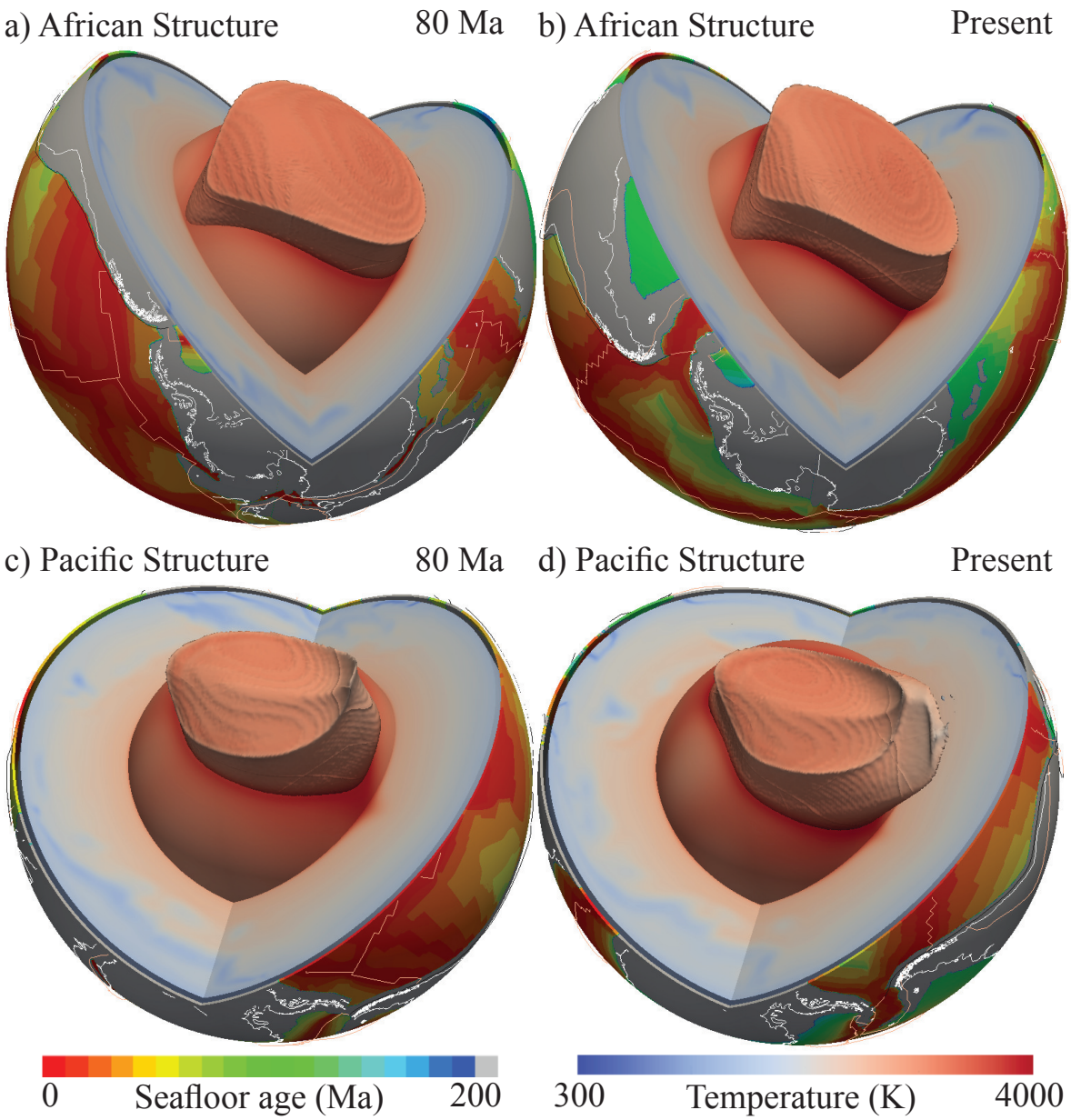

Figure 9. 3-D view of the domes (Model EX5). African structure at (a) 80 Ma, (b) Present. Pacific structure at (c) 80 Ma, (d) Present. Ridges and transform faults are represented by red lines and subduction zones are represented by black lines. Non-oceanic regions are dark grey and reconstructed continents with present-day shorelines are shown in white.

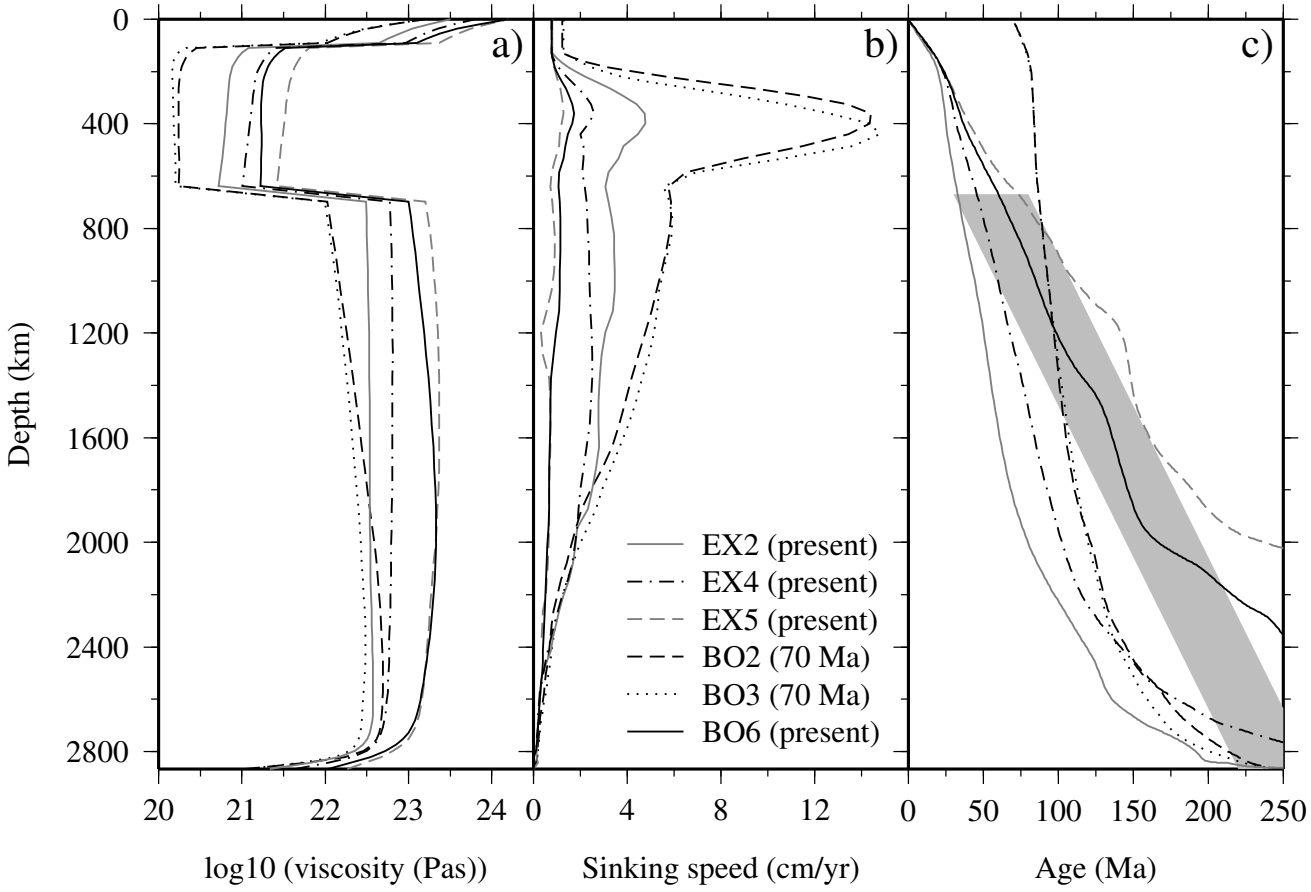

Figure 10. Radial profiles for (a) Viscosity, (b) Slab sinking speed, (c) Approximate age of subducted material versus depth, for EX2, EX4, EX5, BO6 at present day, and BO2, BO3 at 70 Ma. For depths > 2000 km the average viscosity may be reduced by the hot domes. Sinking speed is determined from positive density anomalies that are greater than 25% of the maximum positive density anomaly at each depth and time [e.g., *Steinberger and Torsvik*, 2010]. We set the velocities for depths < 128 km to the value at 128 km depth because they are influenced by data assimilation. The age-depth relation is computed by integrating the time- and depth-dependent slab sinking speed and the grey-shaded region shows a geological estimate [*van der Meer et al.*, 2010].